

Sound generation by turbulent boundary-layer flow over small steps

MINSUK JI AND MENG WANG[†]

Center for Flow Physics and Control, Department of Aerospace and Mechanical Engineering,
University of Notre Dame, Notre Dame, IN 46556, USA

(Received 4 August 2008; revised 26 January 2010; accepted 26 January 2010;
first published online 11 May 2010)

The aeroacoustics of low-Mach-number boundary-layer flow over backward and forward facing steps is studied using large-eddy simulation and Lighthill's theory. The Reynolds number based on the step height and free-stream velocity ranges from 21 000 to 328 as the step height is varied from 53 % to 0.83 % of the unperturbed boundary layer thickness at the step. For the largest step size, statistics of wall pressure fluctuations such as the root mean square values and frequency spectral density yield favourable comparisons with available experimental measurements. A low-frequency Green's function for the step geometry, valid for an acoustically compact step height, is employed to evaluate the volume integral in the solution to Lighthill's equation. Consistent with the result of previous theoretical studies, the steps act primarily as a dipole source aligned in the streamwise direction. The sound from the forward step is shown to be significantly louder than that from the backward step and the underlying reason is analysed in terms of source strength and distribution relative to the Green's function. The forward step generates stronger sources in regions closer to the step corner, which is heavily weighted by the Green's function. A detailed analysis of flow field and Green's function weighted sources reveals that the backward step generates sound mainly through a diffraction mechanism, while the forward step generates sound through a combination of diffraction and turbulence modification by the step. As the step height decreases, the difference in noise level between forward and backward steps is much reduced as turbulence modification becomes less significant.

1. Introduction

Non-uniform surfaces of road, flight and marine vehicles can disturb the turbulent boundary layer around the body, causing sound radiation and large surface pressure fluctuations, which act as a source of structural vibration. Irregularities on aircraft surfaces are one such example, where unsteady pressure fluctuations induced by rivet heads, window cutouts and lap joints are a source of interior cabin noise (Kargus & Lauchle 1997; Howe 1998; Lauchle & Kargus 2000). Similarly, gaps, ribs and panel mismatches are routinely found on marine vehicles. In order to control flow-induced sound it is necessary to understand the nature of unsteady surface pressure and mechanisms for noise production from surface inhomogeneities immersed in turbulent flow. In this regard, the backward and forward facing steps provide an ideal framework for studying the relevant source processes because their geometry is simple yet they possess complex flow features such as separation and reattachment, which lead to

[†] Email address for correspondence: M.Wang@nd.edu

high levels of flow unsteadiness. Although the step flows – especially the backward facing step – have been a subject of extensive research for the past few decades, the focus has mainly been on the hydrodynamic aspects with rather limited acoustical implications (see e.g. Bradshaw & Wong 1972; Moss & Baker 1980; Chandrsuda & Bradshaw 1981; Eaton & Johnston 1981; Le, Moin & Kim 1997).

Wall pressure fluctuations in flows over backward and forward facing steps have been experimentally investigated by a number of researchers (e.g. Mohsen 1968; Farabee & Casarella 1984, 1986; Efimtsov *et al.* 1999, 2000; Lee & Sung 2001; Camussi, Guj & Ragni 2006; Largeau & Moriniere 2007). Flow separation and reattachment give rise to larger unsteady pressure fluctuations than those beneath attached turbulent boundary layers, and their maximum occurs near the reattachment location. Compared to the flat-plate boundary layer with zero pressure gradient, the peak root mean square (r.m.s.) values of pressure fluctuations are 5 and 10 times larger (Farabee & Casarella 1984, 1986), and the frequency spectra levels are up to 20 and 30 dB larger (Efimtsov *et al.* 1999, 2000) for the backward and forward facing steps, respectively. The increase in wall pressure fluctuations is largely due to the amplification of energy in the low-frequency range of the pressure spectrum, which is caused by organized low-frequency velocity fluctuations in the free shear layer and recirculation bubble (Farabee & Casarella 1986; Lee & Sung 2001; Largeau & Moriniere 2007).

Experimental studies of sound radiation from flow over steps are relatively fewer and more recent. Farabee & Zoccola (1998) measured the noise from flow over backward and forward facing steps for free-stream velocities of 25.5 and 40.7 m s⁻¹, step heights of 0.76 and 1.40 cm and boundary layer thickness of approximately twice the step height. They reported that the forward step was noisier than the backward step; the noise level from the forward step was generally 5 dB above the background level across all frequencies while the backward step did not produce noise greater than the background level. Sound radiation from wall-jet flow over a backward facing step was studied by Jacob *et al.* (2001) for the Mach number range of approximately 0.1–0.24 based on the maximum mean streamwise velocity above the step, and step height up to 6 cm. By applying acoustic source localization method, which constructs a best fitting streamwise distribution of monopoles according to measurements, they found maximum source strength at 2.5 step heights downstream of the step, where the strongest turbulence level was also measured. Note that this localization does not account for the edge-scattering effect, which makes the source region closer to the top corner of the step radiate more efficiently. Their far-field sound measurements indicated strong upstream and downstream directivity; it became more dipole-like as the step height and free-stream velocity were decreased, making the step more acoustically compact. Leclercq *et al.* (2001) studied the acoustic field for low-Mach-number flow over a large-aspect-ratio block (10 step heights long). Using the same localization technique as in Jacob *et al.* (2001), they showed that the leading forward facing step was the dominant source. Becker *et al.* (2005) measured the sound field from flow over a forward facing step with step height of 1.2 cm and free-stream velocity of 10–35 m s⁻¹. They found that the resulting sound pressure level was up to 10 dB higher than that of flow over a flat plate within the frequency range from 1 to 10 kHz. Their experimental data exhibited a sound power level according to the sixth power of the flow speed, suggesting a dipole-like behaviour.

A number of theoretical studies examined the sound generated by low-Mach-number flows over a step (e.g. Conlisk & Veley 1985; Dhanak & Gundlapalli 1992; Howe 1989, 1997, 1998). Conlisk & Veley (1985) and Dhanak & Gundlapalli (1992)

considered the motion of line vortices in an inviscid flow over a forward facing step and examined its effect on radiated sound. Howe (1989, 1998) analysed the sound from a forward step produced by the diffraction of a frozen boundary-layer pressure field. These studies employed inviscid approximations, therefore ignoring the flow separation at the step which inevitably generates additional vortices that may contribute to the sound. Howe (1997) modelled the flow separation at forward and backward steps and found that the effect of separation became smaller as the step height decreased with respect to the boundary layer thickness. In a realistic step flow, noise is generated by not only diffraction of hydrodynamic pressure, but also the distortion of incoming turbulent eddies and generation of new turbulence structures by the steps. The latter are sources of self noise, and a full account of them requires a viscous flow computation.

There are no computational studies, to the authors' knowledge, of wall pressure fluctuations in flow over steps although studies of other separated flows exist (see e.g. Na & Moin 1998; Kim & Sung 2006). On the other hand, a few computational studies have been conducted recently to investigate the flow-induced noise from steps. Addad *et al.* (2003) performed large-eddy simulation (LES), with a commercial computational fluid dynamics code, of the flow over a large-aspect-ratio block considered experimentally by Leclercq *et al.* (2001), and examined the acoustic source terms for linearized Euler equations. Consistent with the findings of Leclercq *et al.* (2001), their results showed that the backward step was a significantly weaker source of noise than the forward step although it should be pointed out that the flow over the backward step was largely influenced by the upstream forward step. Becker *et al.* (2005) utilized LES for the flow field while applying finite element method to solve for the acoustic field the inhomogeneous wave equation from Lighthill's acoustic analogy (Lighthill 1952). Their contour plot of the instantaneous acoustic pressure field around the step showed a predominantly dipole directivity pattern. Ali *et al.* (2007) performed LES for a forward facing step and computed the sound field using linearized Euler equations.

The aforementioned approaches based on numerical solutions of linearized Euler equations and the Lighthill equation allow flexible treatment of solid boundaries and, in the case of linearized Euler equations, incorporation of the effect of flow on wave propagation. However, they are prone to numerical errors, particularly for low-Mach-number flows, because the true source characteristics (e.g. dipole, quadrupole) are not represented in the original equations. The importance of representing the correct source characters in a numerical evaluation was stressed by Crighton (1975) and more recently by Wang, Freund & Lele (2006). Furthermore, it is difficult to assess the relative importance of different source locations in such numerical solutions because the enhanced radiation efficiency by surface scattering is not known explicitly. For better numerical accuracy and physical insight, it is generally preferable (when feasible) to employ an integral solution to the Lighthill equation with an appropriate Green's function, obtained analytically or numerically. This is the approach taken here.

In the present work, LES is employed to study the aeroacoustics of low-Mach-number boundary-layer flows over backward and forward facing steps. The focus is on steps that are small relative to the boundary layer thickness. Acoustic calculations are carried out using Lighthill's analogy (Lighthill 1952) with a Green's function tailored to the step geometry for acoustically compact step height (Howe 1989, 2003). This approach offers the advantage that the source characteristics are represented correctly by analytical means, thus fostering numerical accuracy. It also facilitates

easy identification of important source regions with account for the effect of Green's function. The use of realistic turbulent source terms generated by LES with the hard-wall Green's function allows inclusion in the calculation of all potential source processes, including the diffraction and distortion of incoming turbulence, unsteady separation and reattachment of shear layers and vortex shedding.

Baseline simulations, with step height equal to 53 % of the boundary layer thickness and Reynolds number of 21 000 based on step height, are first carried out and the results are compared with experimental data of Farabee and colleagues (Farabee & Casarella 1984, 1986; Farabee & Zoccola 1998). The objectives are to validate the LES results in terms of basic flow statistics and frequency spectra of wall pressure fluctuations, and to better understand the noise production mechanisms and important source regions. The results are used to explain the disparity in noise levels noted by Farabee & Zoccola (1998) between the backward and forward steps in terms of source and Green's function distributions. The forward step produces stronger sound because of stronger sources near the step upper corner, which is weighted most heavily by the Green's function.

A further objective of the study is to examine the effect of step height on sound generation. Most previous studies mentioned above dealt with steps whose size was comparable to or larger than the incoming turbulent boundary layer thickness. However, surface discontinuities such as gaps and panel mismatches found on marine and air vehicles are of a much smaller size – typically a few per cent of the boundary layer thickness. Despite the small size, they can significantly affect the flow noise through diffraction and turbulence modification. To elucidate the effect of step size on sound generation and source mechanisms, three additional step heights, which are 13 %, 3.3 % and 0.83 % of the boundary layer thickness, are considered for both backward and forward steps. The extent to which diffraction and source modifications by the step impact sound generation is examined through source field analysis along with the Green's function. It is found that step height affects the backward-step sound level mainly through diffraction (Green's function), whereas it affects the forward-step sound through a combination of diffraction and source modification. As the step height decreases, the difference in sound level between backward and forward steps is reduced as source modification becomes less significant.

2. Computational methodology

Eight simulations, which comprise backward and forward facing steps of four different heights, were carried out. In this section and §§3 and 4, the baseline simulations corresponding to the largest steps are described. Smaller step simulations are performed with the same method and requirement for spatial and temporal resolutions, and are discussed in §5.

The parameters used in the baseline simulations were chosen to closely match the experimental conditions of Farabee and colleagues (Farabee & Casarella 1984, 1986; Farabee & Zoccola 1998). Experimental measurements were taken in the open-jet test section of an anechoic wind tunnel and the Reynolds number Re_h , based on the step height h and free-stream velocity U_0 , ranged from 21 000 to 37 000. The boundary layer thickness upstream of flow separation varied from $1.0h$ to $2.4h$ and the Mach number was in the range 0.075–0.12. The Reynolds number Re_h is selected to be 21 000 in the simulation based on the amount of available data for comparisons and simulation affordability. The unperturbed (i.e. without the step) boundary layer thickness δ at the step location is $1.88h$, or the step height is 53 % of the boundary

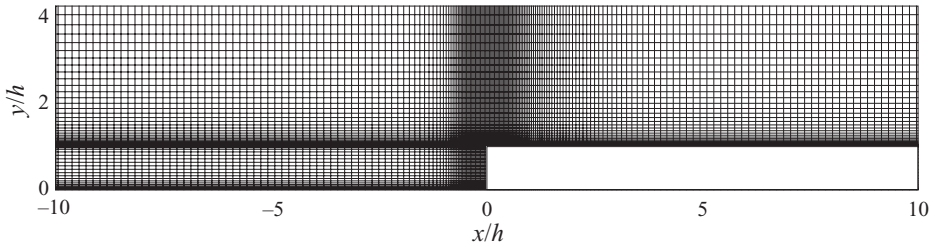


FIGURE 1. A portion of computational domain and mesh (every third line shown in each direction) at a given spanwise plane for the largest forward step.

layer thickness. The Reynolds number based on the unperturbed momentum thickness at the step is $Re_\theta = 4755$. In dimensional units, $h = 1.27$ cm and $U_0 \simeq 25$ m s⁻¹.

2.1. Computational domain and grid

Figure 1 shows a close-up of the computational domain around the baseline forward facing step at a spanwise plane. The computational domain size is $L_x = 40h$, $L_y = 30h$ and $L_z = 4h$ in the streamwise (x), wall-normal (y) and spanwise (z) directions, respectively. The streamwise domain length is equally divided between upstream and downstream regions of the step (each with $20h$) and the coordinate system origin coincides with the lower corner of the step in the mid-span plane. Previous numerical studies of turbulent flow over a backward facing step (Akselvoll & Moin 1995; Le *et al.* 1997) employed a similar domain size: $10h$, $20h$ and $4h$ in the step upstream, downstream and spanwise directions, respectively; domain height was limited to $6h$ since they were closed channel simulations. As will be discussed in §3, the current computational domain size is considered adequate for the objective of studying wall pressure fluctuations and flow-induced noise.

The grid used in the simulations is non-uniform in the streamwise and wall-normal directions, and uniform in the spanwise direction (figure 1). The number of grid points is $897 \times 261 \times 129$ ($N_x \times N_y \times N_z$), and the maximum grid stretching ratio is 1.01 and 1.09 in the streamwise and wall-normal directions, respectively. When scaled by the wall quantities at the inlet, the streamwise grid spacing Δx^+ is mostly between 8 and 44, with its minimum occurring at the step face. In order to reduce the number of points, the grid far downstream of the step is further stretched from $\Delta x^+ = 44$ at $x/h = 10$ to 79 at $x/h = 20$. In the wall-normal direction, Δy^+ ranges from 1.7 at the step upper and lower surfaces to 44 at $y/h \simeq 3$, the approximate edge of the boundary layer above the step. The spanwise grid spacing Δz^+ is 25. These grid spacings are comparable to those used in the LES of Akselvoll & Moin (1995) for a backward facing step, whose results compared well with those from the direct numerical simulation (DNS) of Le *et al.* (1997). Note that, since a staggered grid is used, the first off-wall nodes for the velocity components parallel to walls are defined at half the grid spacing mentioned above (i.e. $\Delta x^+ = 4$ and $\Delta y^+ = 0.85$). This computational grid was found to be adequate for accurately predicting the flow and acoustic quantities of interest. A comparison of simulation results with those obtained on a coarse mesh, which is a factor of two coarser in each direction, showed good agreement. The acoustic spectra differed by no more than 1.3 dB in the low to intermediate frequency range not affected by the grid cutoff.

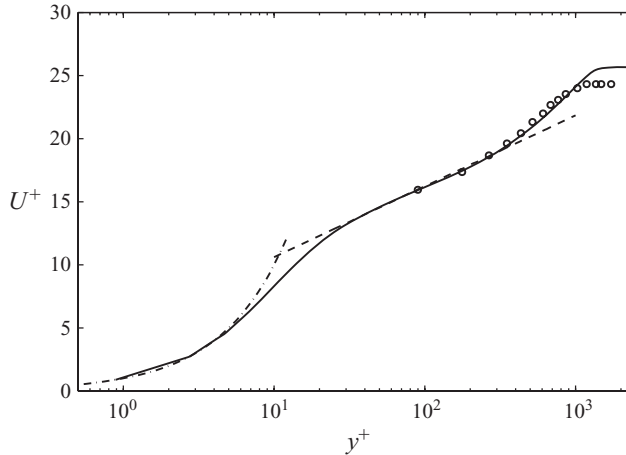


FIGURE 2. Mean streamwise velocity profile in wall units for the inflow turbulent boundary layer. —, LES at $Re_\theta = 4100$; \circ , Farabee & Casarella (1984) at $Re_\theta = 2541$; — · —, $U^+ = y^+$; ----, $U^+ = (1/0.41) \ln y^+ + 5.0$.

2.2. Numerical method and boundary conditions

The numerical algorithm used in this study is described in detail by You *et al.* (2004). The spatially filtered unsteady incompressible Navier–Stokes equations are solved in conjunction with the dynamic Smagorinsky model of Germano *et al.* (1991) with Lilly’s modification (Lilly 1992). The governing equations are spatially discretized with a second-order central-difference scheme on a staggered grid. The solution is advanced in time using a fractional step method with a semi-implicit approach: viscous terms are treated implicitly with the second-order Crank–Nicolson scheme and convective terms are treated explicitly with a third-order Runge–Kutta scheme. A constant Courant–Friedrichs–Lewy number of 1.0 is employed, resulting in an average Δt of $4.50 \times 10^{-3} h/U_0$ and $1.71 \times 10^{-3} h/U_0$ for the backward and forward facing steps, respectively. The pressure Poisson equation is solved with a multigrid iterative method combined with a Fourier collocation method in the spanwise direction. The numerical code is non-dissipative and energy conservative. It has been successfully used in the past to compute trailing-edge aeroacoustics (Wang & Moin 2000; Wang *et al.* 2009) and tip-clearance flow (You *et al.* 2007), among others. The current simulation employs a Cartesian grid approach with the immersed boundary method of Fadlun *et al.* (2000) to enforce the no-slip boundary condition on the step surfaces.

Adopting the method of Lund, Wu & Squires (1998), a separate LES of a flat-plate turbulent boundary layer at $Re_\theta = 4100$ was carried out to generate realistic turbulent inflow data as inlet boundary conditions for the main simulations. Shown in figure 2 is the mean streamwise velocity profile in wall units at the inlet of the computational domains. A no-slip boundary condition was imposed at the wall, and the periodic boundary condition was used in the spanwise direction. At the top of the domain, a Dirichlet boundary condition $(u, v, w) = (U_0, 0, 0)$ was employed. With the wall-normal computational domain size of $L_y = 30h$, the expansion and contraction ratios are 1.034 and 0.967 for the backward and forward steps, respectively. The mean streamwise velocity near the top boundary was within 1% and 3% of the inlet free-stream velocity for the backward and forward steps, respectively. At the exit, a convective outflow boundary condition was used.

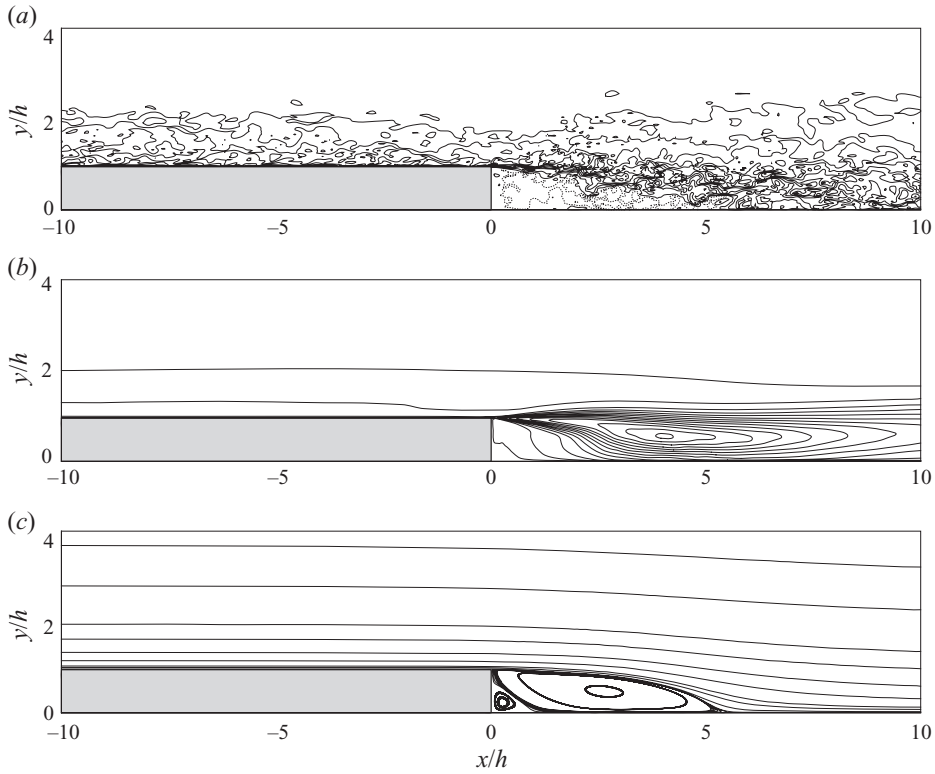


FIGURE 3. Velocity fields for the backward facing step. (a) Instantaneous streamwise velocity u/U_0 , 14 contour levels from -0.25 to 0.95 . Dotted lines denote negative values. (b) Turbulent kinetic energy $(\overline{u^2} + \overline{v^2} + \overline{w^2})/(2U_0^2)$, 14 contour levels from 0.002 to 0.03 . (c) Mean streamlines.

3. Flow simulation results

3.1. Flow field

The velocity fields for the backward facing step are shown in figure 3 for $-10 \leq x/h \leq 10$. The contours of instantaneous streamwise velocity, u/U_0 , at a spanwise location (figure 3a) show that the turbulent boundary layer separates at the corner of the step, forms a free shear layer and reattaches at about 5 step heights downstream of the step. Underneath the shear layer, u/U_0 is largely negative (dotted lines) and small in magnitude. Figure 3(b) shows contours of turbulent kinetic energy, $(\overline{u^2} + \overline{v^2} + \overline{w^2})/(2U_0^2)$, and illustrates the extent of unsteadiness in different regions of the flow. Maximum turbulent kinetic energy level of 0.03 is seen in the region around $(x/h, y/h) = (4.0, 0.6)$, along the rear part of the shear layer. The mean streamlines obtained by temporal and spanwise spatial averaging (figure 3c) indicate that two separation bubbles are formed. The primary bubble extends from the step face to approximately 5.7 step heights downstream, and the smaller secondary bubble extends to 1.07 step heights downstream.

Figure 4(a-c) displays the instantaneous streamwise velocity contours, turbulent kinetic energy contours and the mean streamlines, respectively, for the case of forward facing step. The turbulent boundary layer is deflected upward as the step is approached, detaches at the step corner to form a shear layer above the step, and reattaches to the wall soon afterwards. Regions of negative u/U_0 occur in front of

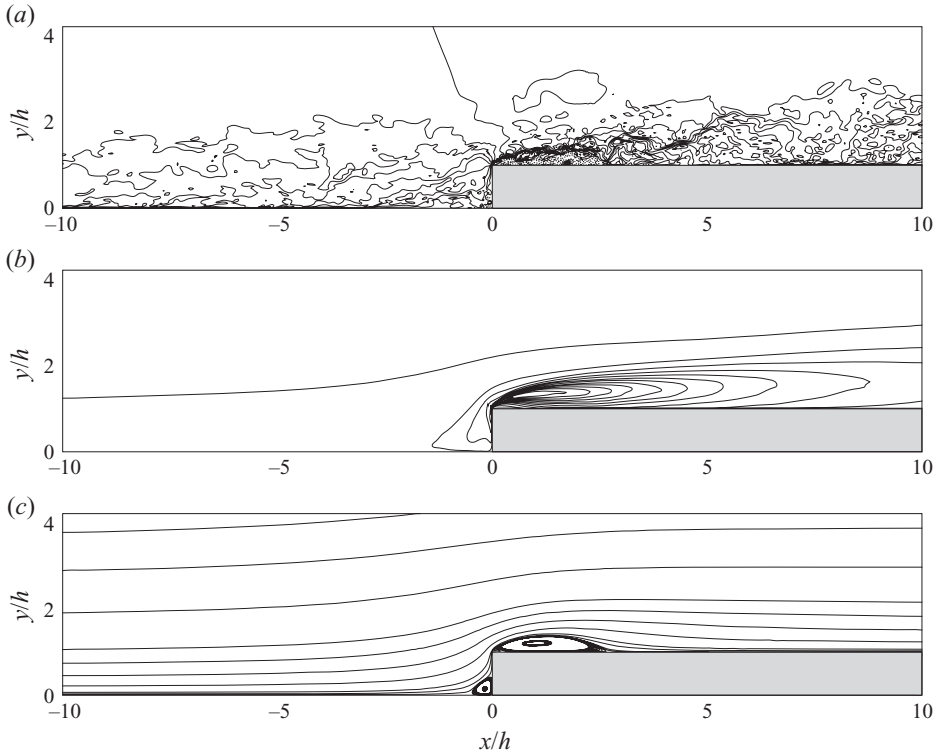


FIGURE 4. Velocity fields for the forward facing step. (a) Instantaneous streamwise velocity u/U_0 , 14 contour levels from -0.45 to 1.15 . Dotted lines denote negative values. (b) Turbulent kinetic energy $(\overline{u'^2} + \overline{v'^2} + \overline{w'^2})/(2U_0^2)$, 14 contour levels from 0.002 to 0.1 . (c) Mean streamlines.

the step and below the shear layer. In figure 4(b), maximum turbulent kinetic energy level of 0.1 is seen along the front part of the free shear layer in the region near $(x/h, y/h) = (0.2, 1.15)$. Mean streamlines show two recirculation bubbles (figure 4c). The small separation bubble in front of the step has a size of $0.58h$ and $0.46h$ in the x and y directions and the larger one above the step extends to approximately 3 step heights downstream.

Although flows over backward and forward facing steps share some common features, such as separation and reattachment of boundary layer and formation of shear layer and recirculation bubbles, their characteristics are very different, which is of significance for wall pressure fluctuations and flow-induced noise. Firstly, the extent of flow unsteadiness differs, as indicated by turbulent kinetic energy magnitudes. The maximum turbulent kinetic energy for the forward step is more than three times that for the backward step. Velocity field acts as a source for the pressure Poisson equation and Lighthill's equation, and as will be seen later, the wall pressure fluctuations and sound radiation are greater for the forward facing step case. Secondly, the location where maximum velocity fluctuations occur is closer to the top step corner for the forward step than for the backward step. This is due to the smaller size and location of the primary recirculation bubble and the strong upward momentum near the corner of the forward facing step. In §4, its consequences on radiated sound will be examined.

The wall skin-friction coefficient $C_f = \tau_w/(\rho U_0^2/2)$ is shown in figure 5 for both steps. The location of zero C_f (or wall-shear stress τ_w) is used to determine the

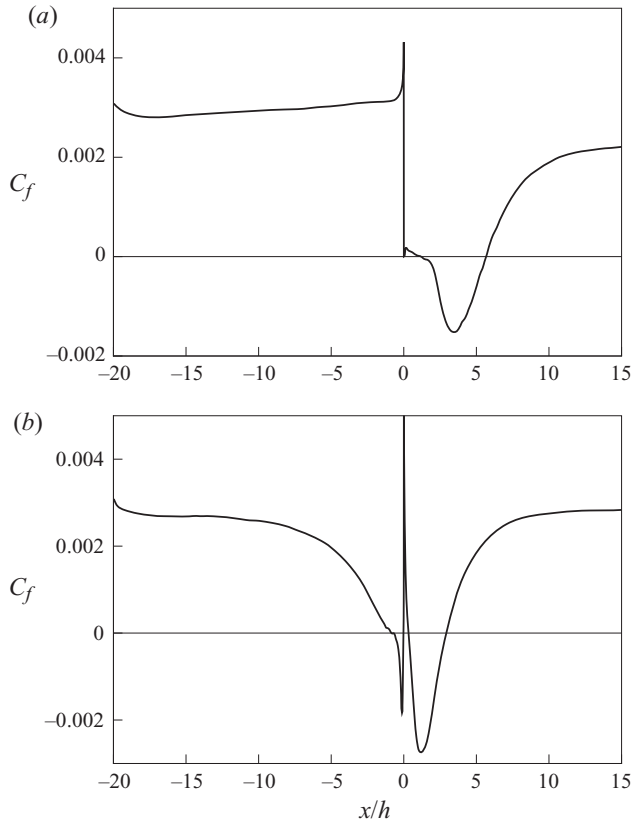


FIGURE 5. Skin-friction coefficient for (a) backward facing step; (b) forward facing step.

mean reattachment length x_r . The separated flow over the backward step reattaches at 5.68 step heights downstream of the step, 5% smaller than $x_r/h \simeq 6$ as noted by Farabee & Casarella (1984, 1986). This is considered satisfactory given experimental uncertainties. Badri Narayanan, Khadgi & Viswanath (1974) observed $x_r/h \simeq 5.6$ in a closed channel with an expansion ratio of 1.008. For the forward facing step, the current simulation predicts $x_r/h = 2.93$ while Farabee & Casarella (1984, 1986) observed $x_r/h \simeq 3$; again the LES prediction is reasonable. Minimum C_f values of -0.0015 and -0.0027 occur at $x/h = 3.47$ for the backward step and at $x/h = 1.18$ for the forward step, respectively. This indicates the backflow in the recirculation zone of the forward facing step is stronger. The C_f distribution shows that the grid spacing in wall units based on the inlet condition is a conservative estimate, as C_f (hence, $u_\tau/U_0 = \sqrt{C_f/2}$) at the inlet is the largest except at a few points near the singular step corner.

Distribution of mean wall pressure coefficient C_p is shown in figure 6. Solid lines are from the current LES, and symbols are from the experiment of Farabee & Casarella (1984, 1986). To examine the effect of computational domain size, the results from a smaller-domain ($20h \times 20h \times 4h$) simulations are plotted as dashed lines. For the backward facing step (figure 6a), the largest discrepancy between the LES and the experiment is seen for $x/h < 0$. This is likely due to a limited computational domain size upstream of the step; experimental data show a steep gradient of C_p at $x/h = -20$ while computational results display flatter curves. The large difference between the

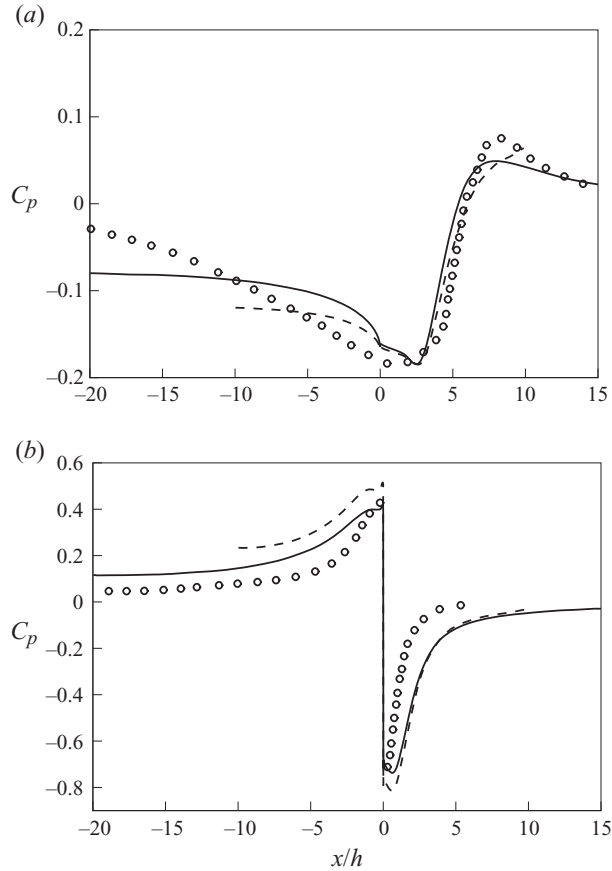


FIGURE 6. Pressure coefficient distribution for (a) backward facing step; (b) forward facing step. —, LES with larger domain; ----, LES with smaller domain; \circ , Farabee & Casarella (1984).

two simulations in this region corroborates this explanation. Despite the differences in the upstream values of C_p , the two simulations agree well for $x/h \geq 0$ except for the region close to the exit boundary of the small domain, where the solution is degraded by the approximate boundary condition. The C_p curves immediately downstream of the step show a qualitatively different behaviour compared to experiment. LES predicts a fall-off region $0 \leq x/h \leq 2.5$, whereas the experiment shows no such region; the computational results, which show a maximum suction pressure inside the recirculation bubble ($x/h = 2.5$), are physically more realistic and also observed in other experiments (see e.g. Moss & Baker 1980). For the forward facing step (figure 6b), the upstream discrepancy is not as pronounced, but the need for a larger computational domain is still acknowledged. Downstream of the step, the computations predict a fall-off region $0 \leq x/h \leq 0.65$ with maximum suction pressure inside the recirculation bubble ($x/h = 0.65$), but the experiment fails to measure it. Similar fall-off region was also observed by Moss & Baker (1980). The two simulation results compare well for $x/h \geq 0$ except for the magnitude of the minimum C_p . The slope of pressure recovery downstream of the step differs between the computation and the experiment. This is puzzling given that the prediction of bubble size is in good agreement with the experimental value.

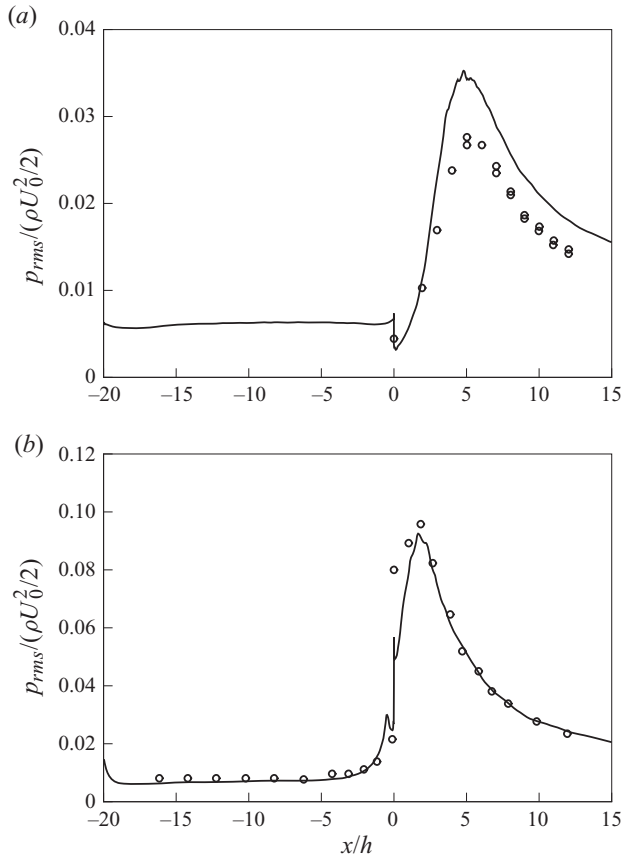


FIGURE 7. Root mean square of wall pressure fluctuations for (a) backward facing step; (b) forward facing step. —, LES; \circ , Farabee & Casarella (1984).

Although the current computational domain size is not ideal, the largest discrepancy in C_p distributions is found in the upstream of the step, and we are mostly interested in modification of the flow field by the step (i.e. $x/h \geq 0$). As it will be seen in §3.2, the r.m.s. of wall pressure fluctuations agree well with experiments (even in the upstream of the steps), indicating insensitivity to the mean C_p . Given the already large grid size in the simulations, and the uncertainty in the experimental C_p data, the current domain size is considered acceptable for the purpose of examining wall pressure fluctuations and flow-induced noise.

3.2. Wall pressure fluctuations

Figure 7 shows the streamwise distribution of the r.m.s. of wall pressure fluctuations normalized by the free-stream dynamic pressure ($\rho U_0^2/2$). Solid lines represent the results from the LES and symbols from the experiment (Farabee & Casarella 1984). For the backward facing step (figure 7a), the peak r.m.s. pressure of 0.035 occurs at $x/h = 4.84$, slightly ahead of the reattachment location ($x_r/h = 5.68$), which agrees with the experimental data of Farabee & Casarella (1984) and others (Lee & Sung 2001 and the references therein). The simulations slightly overpredict the r.m.s. pressure near and downstream of its peak, but the overall agreement with experimental values is good.

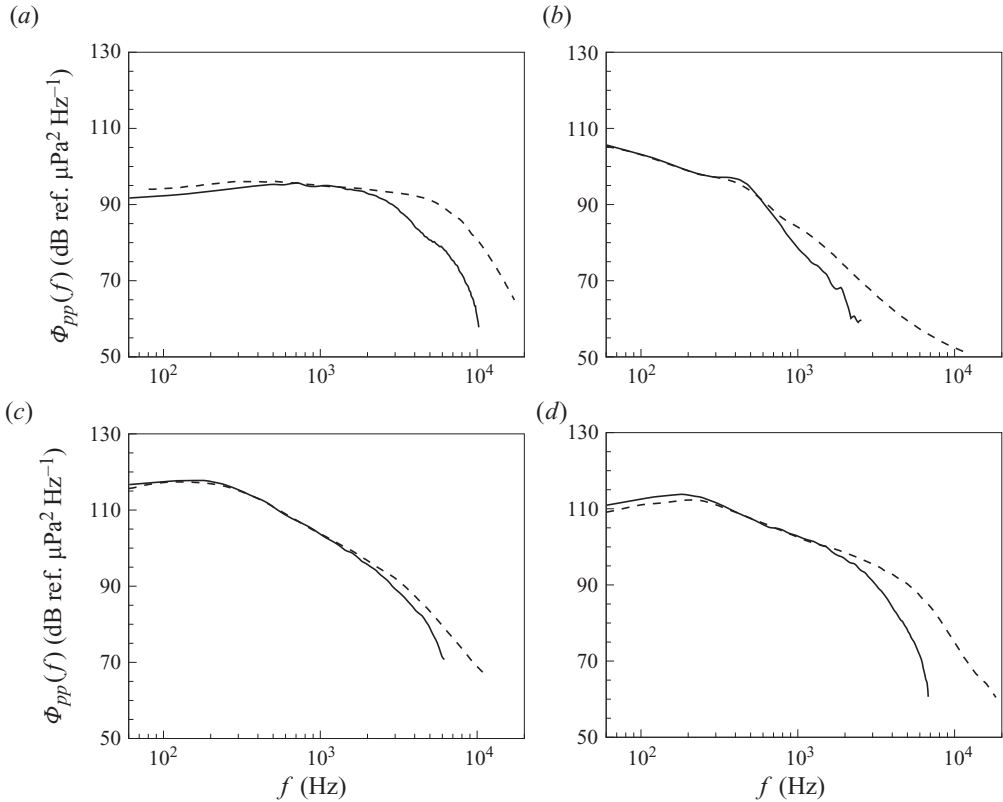


FIGURE 8. Frequency spectra of wall pressure fluctuations for the backward facing step at four streamwise locations: (a) $x/h = -16$; (b) $x/h = 1$; (c) $x/h = 6$; (d) $x/h = 10$. —, LES; ----, Farabee & Casarella (1986).

The r.m.s. pressure fluctuations for the forward facing step (figure 7b) generally agree well between the LES and experiments (Farabee & Casarella 1984). It is interesting to observe that the r.m.s. pressure upstream of the step is predicted well by LES even though the adverse mean pressure gradient deviates from experimental data. The location ($x/h = 1.69$) and magnitude ($= 0.092$) of the peak r.m.s. pressure agree fairly well with experiments.

Frequency spectra of wall pressure fluctuations are shown in figures 8 and 9 for the backward and forward facing steps at four and six different streamwise locations, respectively. In order to facilitate a comparison with experimental data, the spectra were converted to dimensional quantities using the parameters used in the experiments. Overall, a good agreement with experimental measurements is obtained for both steps at all locations. Changes in spectral level and shape as a function of streamwise location are well captured by LES over a wide range of frequencies. The computation predicts an early fall-off at higher frequencies, which is a characteristic of LES due to limited grid resolution. It is worth pointing out that the wall pressure fluctuations and radiated sound pressure are generated by the same turbulent source field. In fact, the dominant source terms in the Lighthill equation (see §4.1) are the same as source terms in the Poisson equation for hydrodynamic pressure. Therefore, the accurate prediction of the wall pressure spectra is indicative of the quality of the acoustic source data generated by LES.

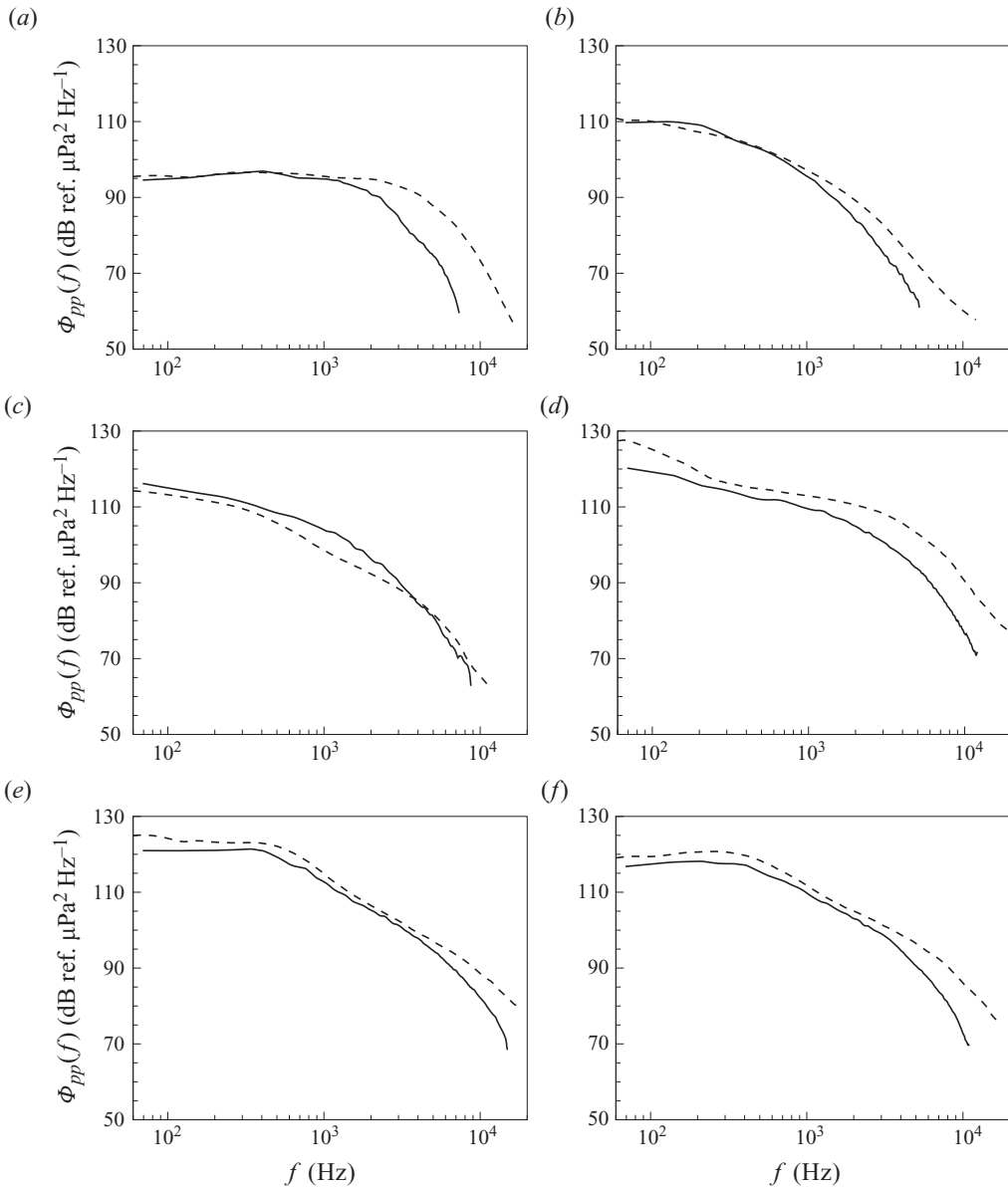


FIGURE 9. Frequency spectra of wall pressure fluctuations for the forward facing step at six streamwise locations: (a) $x/h = -6$; (b) $x/h = -1$; (c) $x/h = 0, y/h = 0$; (d) $x/h = 0, y/h = 1$; (e) $x/h = 2$; (f) $x/h = 4$. —, LES; ----, Farabee & Casarella (1986).

The spectral features in figures 8 and 9 are related to the flow regimes in the following way. At the farthest upstream location shown for the backward facing step (figure 8a), the spectrum is essentially that of a flat-plate turbulent boundary layer. A short distance downstream of the backward facing step (figure 8b), the spectrum shows elevated low-frequency content but little high-frequency energy, suggesting that the pressure fluctuations are dominated by the recirculating flow inside the separation bubble. The pressure level is highest near the reattachment point (figure 8c) and, at low frequencies, is more than 20 dB above that for a flat-plate boundary layer; this is

caused by the shear layer impinging on the wall (Farabee & Casarella 1986; Camussi *et al.* 2006). Past the reattachment location (figure 8*d*), the spectral level is seen to decrease as the reattached boundary layer starts to relax towards the equilibrium turbulent boundary layer.

Similar accounts can be made of the frequency spectra for the forward step. At 6 step heights upstream of the step (figure 9*a*), the spectrum is similar to that of an equilibrium boundary layer. As the step is approached, the adverse mean pressure gradient increases and its effect on the pressure fluctuations is noticeable starting at $x/h \simeq -3$ (figure 7*b*). The increase in pressure level upstream of the step is depicted in figure 9*b*). The pressure fluctuations see a sudden rise from the base to the top of the step (figure 7*b* and figure 9*c,d*) before further increasing to reach the maximum near the reattachment point (figure 9*e*). After the flow reattaches, the spectral level is reduced (figure 9*f*).

Earlier experimental studies on separated and reattaching flows (e.g. Kiya & Sasaki 1983; Cherry, Hillier & Latour 1984) identified frequencies associated with shear layer flapping and vortex shedding. The former was observed in the frequency spectra of wall pressure very near the separation point, $x/x_r \leq 0.2$ (x_r is the reattachment length), and was approximately $f x_r / U_0 \simeq 0.15$. The latter was detected further away from the separation point, $0.55 \leq x/x_r \leq 1.5$, and the wall pressure spectra exhibited a peak near $f x_r / U_0 \simeq 0.6$. When they are converted to a dimensional quantity using the parameters in the present study, the approximate flapping and shedding frequencies are, respectively, 41 and 207 Hz for the backward step, and 79 and 394 Hz for the forward step. Although our data are not sufficient to include the flapping frequencies, the spectra at the vortex-shedding frequencies are computed accurately. Both numerical and experimental curves in figure 8*c*) and figure 8*d*) ($x/h = 6$ and 10) display a peak at approximately 200 Hz, which can be attributed to the vortex shedding (also compare with figure 23 of Cherry *et al.* 1984 and figure 5 of Lee & Sung 2001). Similarly for the forward step, figure 9*e*) and figure 9*f*) ($x/h = 2$ and 4) display a broadband shedding peak at approximately 400 Hz.

4. Flow-induced sound

4.1. Formulation

The far-field sound from the backward and forward steps is calculated in the framework of Lighthill's aeroacoustic theory (Lighthill 1952). The fluctuating pressure $p(\mathbf{x}, t)$ due to flow-generated acoustic waves is governed by

$$\left(\frac{1}{c_0^2} \frac{\partial^2}{\partial t^2} - \nabla^2 \right) p = \frac{\partial^2 T_{ij}}{\partial x_i \partial x_j}, \quad (4.1)$$

where $T_{ij} = \rho u_i u_j + p_{ij} - \delta_{ij} c_0^2 \rho$ is the Lighthill stress tensor and c_0 is the ambient speed of sound. A general solution to the above equation in the frequency domain is given by Goldstein (1976):

$$\hat{p}(\mathbf{x}, \omega) = \int_V \hat{T}_{ij}(\mathbf{y}, \omega) \frac{\partial^2 G}{\partial y_i \partial y_j}(\mathbf{x}, \omega; \mathbf{y}) d^3 \mathbf{y} + \int_S n_j \hat{p}_{ij}(\mathbf{y}, \omega) \frac{\partial G}{\partial y_i}(\mathbf{x}, \omega; \mathbf{y}) d^2 \mathbf{y}, \quad (4.2)$$

where $\hat{(\)}$ represents the Fourier transform of a function, $p_{ij} = p \delta_{ij} - \tau_{ij}$ is the stress tensor including pressure and viscous stress contributions, \mathbf{x} and \mathbf{y} denote the observation and source locations, respectively, and n_j is the solid surface unit normal into the fluid. For low-Mach-number flows without strong temperature

inhomogeneities, the Lighthill stress tensor can be approximated by $T_{ij} \simeq \rho_0 u_i u_j$, where ρ_0 is the ambient density. $G(\mathbf{x}, \omega; \mathbf{y})$ in (4.2) is the three-dimensional Green's function in frequency space and satisfies the Helmholtz equation

$$(\nabla^2 + k^2)G(\mathbf{x}, \omega; \mathbf{y}) = -\delta(\mathbf{x} - \mathbf{y}), \quad (4.3)$$

where $k = \omega/c_0$ is the acoustic wavenumber.

The use of incompressible flow simulations such as the present LES to compute acoustic source terms can be adequate for low-Mach-number flows and advantageous over more expensive compressible flow simulations (Wang *et al.* 2006). However, it generally requires a Green's function specific to a given geometry to enforce the appropriate wall boundary condition for the wave field, and finding such Green's function analytically is generally not possible except for simple geometries. For the present problem, an approximate Green's function can be obtained for step height that is much smaller than the acoustic wavelength, which is the case for a wide range of frequencies in the low-Mach-number turbulence. Howe (1989, 2003) shows that the compact Green's function for the step geometry can be written as (here, shown in the frequency space)

$$G(\mathbf{x}, \omega; \mathbf{y}) = \frac{1}{4\pi} \left(\frac{e^{ik|\mathbf{x}-\mathbf{Y}|}}{|\mathbf{x}-\mathbf{Y}|} + \frac{e^{ik|\mathbf{x}-\mathbf{Y}'|}}{|\mathbf{x}-\mathbf{Y}'|} \right), \quad (4.4)$$

where

$$\begin{aligned} Y_1 &= Y'_1 = Y_1(y_1, y_2), \\ Y_2 &= -Y'_2 = y_2, \\ Y_3 &= Y'_3 = y_3. \end{aligned}$$

The quantity Y_1 satisfies the Laplace equation with $\partial Y_1/\partial n = 0$ on the surface including the step face, approaches y_1 at large distances from the wall, and is thus analogous to the velocity potential for an ideal fluid flow over the step. It is obtained by application of Schwarz–Christoffel transformation (Howe 1989, 2003; see Appendix).

The use of an analytical Green's function like this can foster numerical accuracy because the correct acoustic source characteristics are captured analytically. It also allows easy identification of important source regions by examining the values of the Green's function derivatives as appearing in (4.2) in relation to source distribution. A similar approach has been employed previously to predict trailing-edge noise (Wang & Moin 2000; Wang *et al.* 2009).

When $G(\mathbf{x}, \omega; \mathbf{y})$ from (4.4) is substituted into (4.2), the surface integral can be neglected since $\partial G/\partial n = 0$ on the surface and the viscous shear stress terms are negligible for high-Reynolds-number flows. In order to evaluate the volume integral, we differentiate G twice with respect to y_i and retain only the leading-order terms in $1/r$ (see Appendix) to obtain in the acoustic far field

$$\frac{\partial^2 G}{\partial y_i \partial y_j} = -\frac{ikr_1}{4\pi} \left(\frac{e^{ikr}}{r^2} + \frac{e^{ikr'}}{r'^2} \right) \frac{\partial^2 Y_1}{\partial y_i \partial y_j}, \quad (4.5)$$

where

$$\begin{aligned} r &= |\mathbf{x} - \mathbf{Y}|, \\ r' &= |\mathbf{x} - \mathbf{Y}'|. \end{aligned}$$

The r_1/r^2 factor in (4.5) is readily identified with a dipole aligned in the streamwise direction as expected for an acoustically compact step; this result is consistent with

the conclusions of earlier studies (Howe 1989, 1998). Y_1 depends on y_1 and y_2 only, and therefore $\partial^2 G/\partial y_i \partial y_j = 0$ for i or $j = 3$.

When $\partial^2 G/\partial y_i \partial y_j$ is substituted into the volume integral and rearranged (see Appendix), we obtain

$$\hat{p}(\mathbf{x}, \omega) = -\frac{ik}{2\pi} \frac{e^{ik|\mathbf{x}|} \cos \theta}{|\mathbf{x}|} \hat{D}(\omega), \quad (4.6)$$

where $\cos \theta = r_1/r$, and

$$D(t) = \int \int \frac{\partial^2 Y_1}{\partial y_i \partial y_j} Q_{ij}(y_1, y_2, t) dy_2 dy_1 \quad (4.7)$$

with

$$Q_{ij}(y_1, y_2, t) = \int T_{ij}(\mathbf{y}, t) dy_3. \quad (4.8)$$

$Q_{ij}(y_1, y_2, t)$ is the Lighthill stress tensor $T_{ij}(\mathbf{y}, t)$ integrated over the span of the computational domain. It is assumed that the spanwise coherence length of acoustic source field is smaller than the spanwise computational domain size, which is acoustically compact. The latter is not a significant restriction because, in the mid-plane perpendicular to the step where experimental measurements are often made, the spanwise extent of the source region is always acoustically compact if the observer is sufficiently far from the step. Multiplying \hat{p} with its complex conjugate, the sound pressure spectra is expressed as

$$\Phi_{pa}(\omega) = \frac{k^2 \cos^2 \theta}{4\pi^2 |\mathbf{x}|^2} \Phi_D(\omega), \quad (4.9)$$

where $\Phi_D(\omega)$ is the spectral density of $D(t)$.

4.2. Sound spectra

When computing the acoustic pressure, it is important to ensure that the volume integral is not affected by the truncation of source terms at the integration boundaries (Wang, Lele & Moin 1996; Wang *et al.* 2006). For the current problem where the turbulent boundary layer extends towards the inlet and exit, we check the magnitude of $\partial^2 Y_1/\partial y_i \partial y_j$ since it multiplies the source term (see $D(t)$ in (4.7)). Figure 10 shows the magnitude of $\partial^2 Y_1/\partial y_i \partial y_j$ in logarithmic scale for the forward step case (mirror images about the $x=0$ plane are obtained for the backward step). The $\partial^2 Y_1/\partial y_1^2$ component is not shown in figure 10 since it is identical to $\partial^2 Y_1/\partial y_2^2$ but with an opposite sign, given that Y_1 satisfies the Laplace equation. It is seen that the magnitude peaks at the upper corner of the step and decreases rapidly away from the step by many orders of magnitude. This ensures that the important source region is localized. The volume integral (4.7) is found to converge within the region $-12 \leq x/h \leq 12$ for the backward step and $-3 \leq x/h \leq 3$ for the forward step.

Figure 11 shows the dimensionless sound pressure spectra as a function of frequency for forward and backward facing steps (P_0 is the ambient pressure and $\gamma = c_p/c_v$ is the specific heat ratio). The sound spectral level for the flow over the forward step is higher than that for the backward step by nearly two decades at low frequencies, although the difference decreases at higher frequencies. Note that all quantities used in the normalization are common to both steps, and therefore the observed difference is not due to non-dimensionalization. The result in figure 11 is qualitatively consistent with the experimental observation of Farabee & Zoccola (1998), who measured the

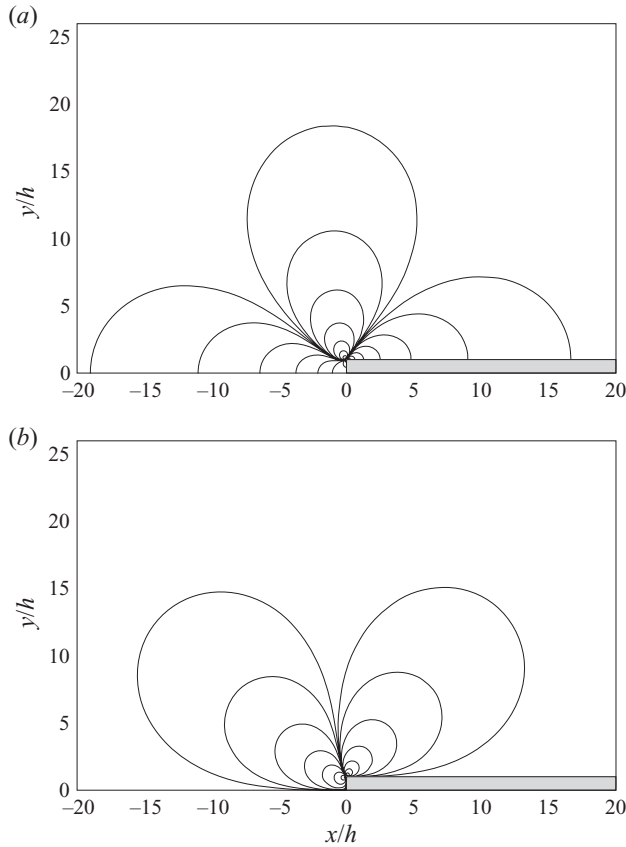


FIGURE 10. Magnitude of the second derivatives of Y_1 in logarithmic scale: (a) $|\partial^2 Y_1 / \partial y_1^2| / h$; (b) $|\partial^2 Y_1 / \partial y_1 \partial y_2| / h$. Contour levels from 10^{-3} to 10^2 with 11 increments.

forward-step noise to be about 5 dB higher than the background level, but failed to measure any noise from the backward step due to poor signal-to-noise ratio. A direct comparison with the experiment cannot be made because experimental measurements were taken directly above the step, where the dominant dipole sound is not present according to (4.6), while in the computation the weaker quadrupole sound has been ignored, leading to no sound above the step. Experimental data were collected in the high-frequency range of 4–90 kHz. In comparison, for a free-stream velocity of $U_0 = 25 \text{ m s}^{-1}$, the frequency range in figure 11 is from 280 Hz to 12 kHz, which corresponds to a wavelength-to-step-height ratio from 95 to 2.2. The acoustic solution becomes less accurate at the high-frequency end because the dipole approximation associated with the low-frequency Green's function (compact step height) is less valid. In the recent measurement by Jacob *et al.* (2001) of sound generated by backward facing steps under a wall jet, the frequency ranged from 192 Hz to 25.6 kHz, corresponding to a wavelength-to-step-height ratio from 35 to 0.3. Their sound pressure measurement showed a more dipole-like directivity for smaller step heights and lower free-stream velocity (i.e. lower Mach number), which make the step more compact acoustically. In the theoretical study of the interaction between a discrete line vortex and steps including the effect of separation, Howe (1997) compared the noise from forward and backward steps. Consistent with the above findings, his

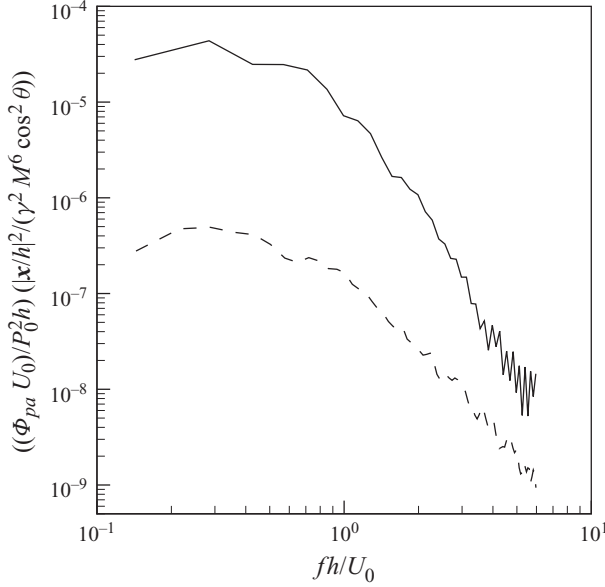


FIGURE 11. Dimensionless sound pressure spectra as a function of frequency. —, forward facing step; ----, backward facing step.

analyses demonstrated that the forward step was a more efficient source of sound. Note that the present dipole formulation does not account for the effect of acoustic convection and refraction by the flow, which can modify the directivity if the Mach number is not small.

In the above calculation, only the source field within the LES domain of spanwise size L_z is considered. In a real configuration with spanwise size $L > L_z$, the total sound spectrum comprises of contributions from L/L_z independent source regions, provided that L_z is no less than the spanwise coherence length of the source field. Therefore, $\Phi_{pa}^{total} \simeq (L/L_z)\Phi_{pa}$. The coherence length of acoustic source field can be estimated by that of fluctuating wall pressure since the same turbulent flow field is responsible for both. The coherence function is defined as

$$\gamma^2(\Delta\mathbf{x}, \omega; \mathbf{x}) = \frac{|\Phi_{pp}(\Delta\mathbf{x}, \omega; \mathbf{x})|^2}{\Phi_{pp}(0, \omega; \mathbf{x})\Phi_{pp}(0, \omega; \mathbf{x} + \Delta\mathbf{x})}, \quad (4.10)$$

where

$$\Phi_{pp}(\Delta\mathbf{x}, \omega; \mathbf{x}) = \frac{1}{2\pi} \int_{-\infty}^{\infty} R_{pp}(\Delta\mathbf{x}, \Delta t; \mathbf{x}) e^{i\omega\Delta t} d(\Delta t) \quad (4.11)$$

is the cross spectrum function and $R_{pp}(\Delta\mathbf{x}, \Delta t; \mathbf{x}) = \langle p(\mathbf{x}, t)p(\mathbf{x} + \Delta\mathbf{x}, t + \Delta t) \rangle$ is the space-time correlation of wall pressure fluctuations. As an example, figure 12 shows the spanwise coherence $\gamma^2(\Delta z, \omega; \mathbf{x})$ for the backward and forward facing steps at $0.2h$ away from the step corner on the upper surface. This location is representative of important source regions as shown in figure 10. The coherence decreases rapidly with spanwise separation for all frequencies, ensuring that the acoustic source field is well decorrelated within the computational domain and that Q_{ij} obtained through the integration in (4.8) is representative of an independent source. Downstream of the reattachment points, low-frequency source structures can be larger than the spanwise

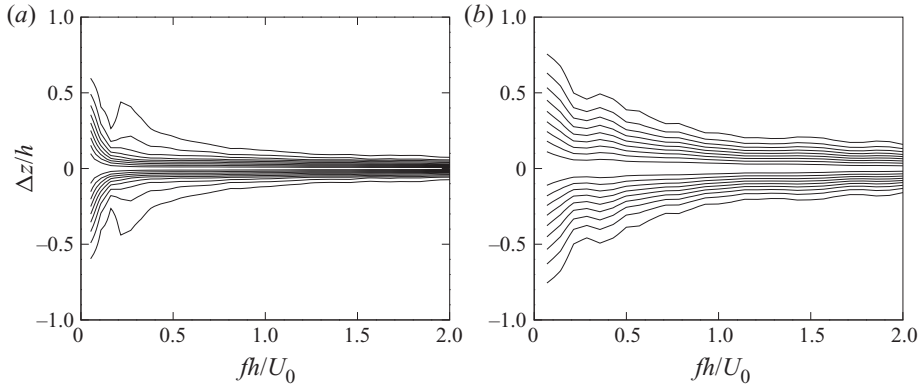


FIGURE 12. Spanwise coherence of wall pressure fluctuations: (a) backward facing step at $x/h = -0.2$; (b) forward facing step at $x/h = 0.2$. Contour levels from 0.1 to 0.9 with 9 increments.

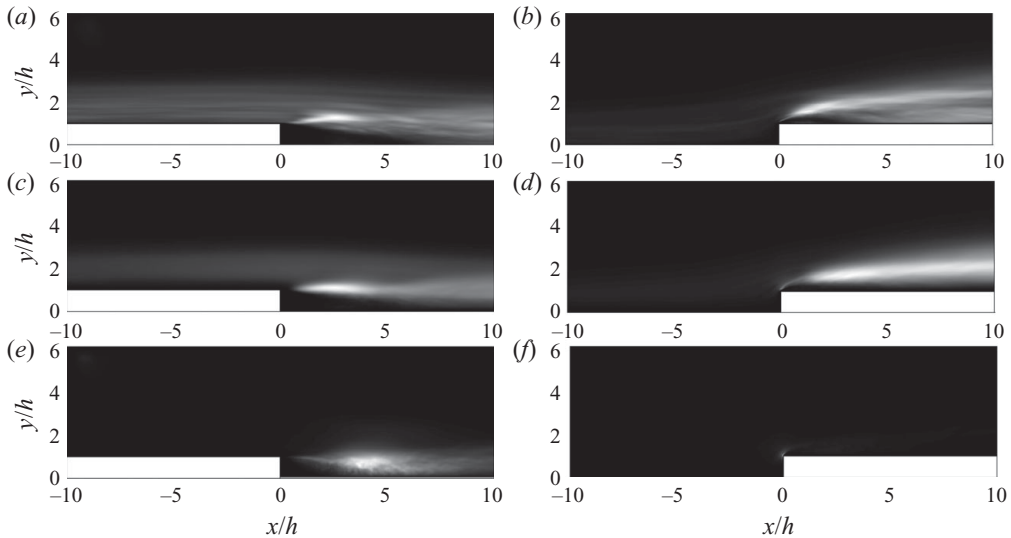


FIGURE 13. Power spectral density of Lighthill stresses $\Phi_{Q_{ij}} U_0 / (\rho_0 U_0^2 h)^2 h$ at $fh/U_0 \simeq 0.30$. (a, c, e) Backward facing step; (b, d, f) forward facing step. (a, b) Q_{11} ; (c, d) $Q_{12} + Q_{21} = 2Q_{12}$; (e, f) Q_{22} . Grey scales range from black (0) to white: (a) 1.45×10^{-2} ; (b) 6.21×10^{-2} ; (c) 2.00×10^{-2} ; (d) 7.15×10^{-2} ; (e) 3.68×10^{-4} ; (f) 3.19×10^{-2} .

domain size, but they are acoustically less important since they are farther away from the step corner.

4.3. Source field

The difference in the noise levels produced by flow over the two steps can be better understood by examining the acoustic source field together with the spatial distribution of the Green's function derivatives (figure 10). Figures 13 and 14 show contours of the power spectral density of spanwise integrated Lighthill stresses, $\Phi_{Q_{ij}} U_0 / (\rho_0 U_0^2 h)^2 h$ at dimensionless frequencies $fh/U_0 \simeq 0.30$ and 2.0 (equivalent to 591 Hz and 3.94 kHz, or acoustic wavelengths of $45h$ and $7h$, for the flow conditions of Farabee & Zoccola 1998), respectively. At both frequencies, flow over the forward

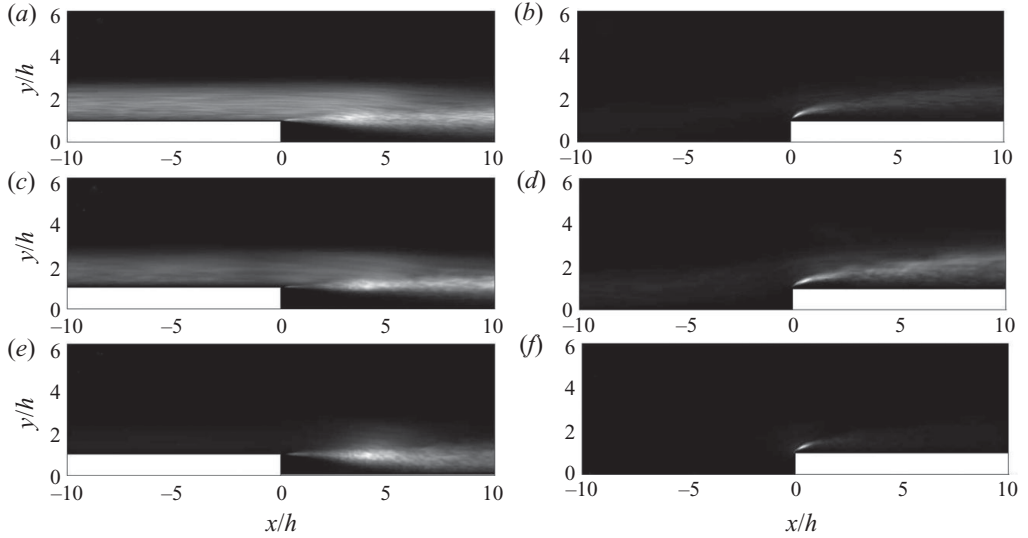


FIGURE 14. Power spectral density of Lighthill stresses $\Phi_{Q_{ij}} U_0 / (\rho_0 U_0^2 h)^2 h$ at $fh/U_0 \simeq 2.0$. (a, c, e) Backward facing step; (b, d, f) forward facing step. (a, b) Q_{11} ; (c, d) $Q_{12} + Q_{21} = 2Q_{12}$; (e, f) Q_{22} . Grey scales range from black (0) to white: (a) 1.74×10^{-4} ; (b) 5.47×10^{-3} ; (c) 7.33×10^{-4} ; (d) 5.31×10^{-3} ; (e) 1.43×10^{-5} ; (f) 1.01×10^{-3} .

step yields acoustic sources of greater magnitude than that over the backward step. As important as the source strength is the spatial distribution of source terms, which differs significantly between the two steps. Regions of intense acoustic source terms are located closer to the upper corner of the step, where the Green's function derivatives are large, in the forward step case than in the backward step case. Similar observations are made at higher frequencies as well.

Figure 15 shows the power spectral density of the Green's function weighted Lighthill stresses

$$\left. \begin{aligned} R_{11}(y_1, y_2, t) &= \frac{\partial^2 Y_1}{\partial y_1^2} Q_{11}, \\ R_{12}(y_1, y_2, t) &= \frac{\partial^2 Y_1}{\partial y_1 \partial y_2} Q_{12} + \frac{\partial^2 Y_1}{\partial y_2 \partial y_1} Q_{21}, \\ R_{22}(y_1, y_2, t) &= \frac{\partial^2 Y_1}{\partial y_2^2} Q_{22} \end{aligned} \right\} \quad (4.12)$$

in logarithmic scale for a six-decade drop in magnitude starting from a maximum. The selected frequency is $fh/U_0 \simeq 0.30$ (same as in figure 13), but similar contour distributions are obtained for $fh/U_0 \simeq 2.0$. In contrast to the raw source distribution in figures 13 and 14, the Green's function weighted source regions are heavily concentrated around the step upper corner for both steps. The contour shape for each component of R_{ij} bears resemblance to that of the corresponding component of the Green's function derivatives $\partial^2 Y_1 / \partial y_i \partial y_j$. The peak magnitude of R_{11} is comparable between backward and forward steps, whereas the maximum R_{22} value is drastically different. This indicates that the strong vertical velocity component induced by the forward facing step plays a large role in producing sound, while the vertical velocity contribution is nearly negligible for the backward step. A comparison of the

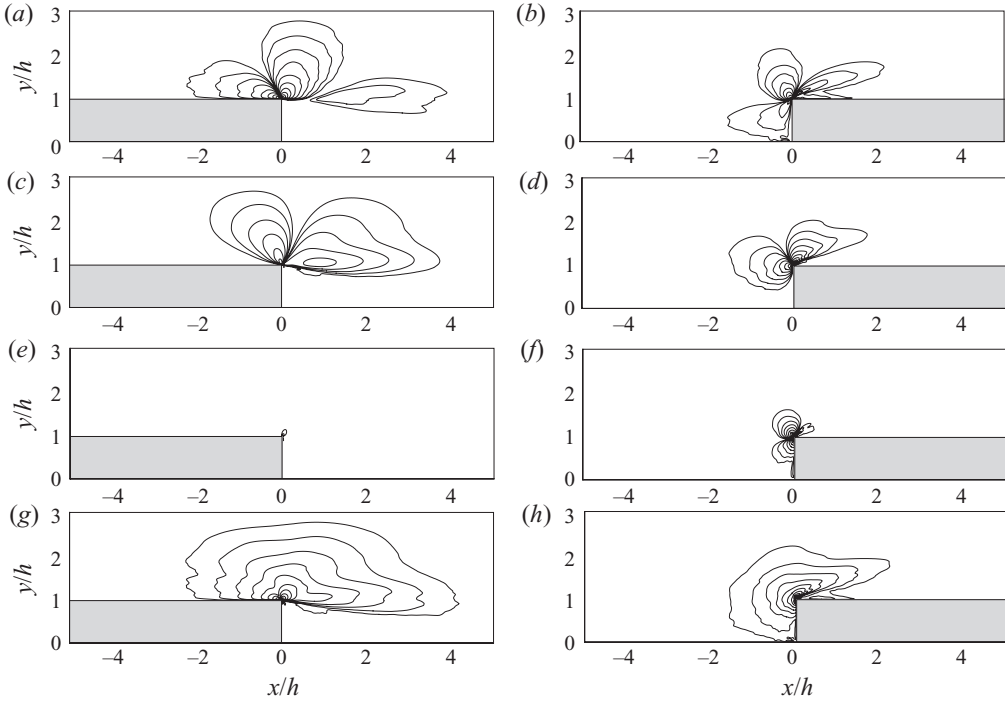


FIGURE 15. Power spectral density of Green's function weighted Lighthill stresses $\Phi_{R_{ij}} U_0 / (\rho_0 U_0^2)^2 h$ at $fh/U_0 \simeq 0.30$. (a, c, e, g) Backward facing step; (b, d, f, h) forward facing step. (a, b) R_{11} ; (c, d) R_{12} ; (e, f) R_{22} ; (g, h) $R = R_{11} + R_{12} + R_{22}$. Thirteen contour levels are plotted in logarithmic scale for left column from 4.30 to 4.30×10^{-6} and for right column from 52.3 to 52.3×10^{-6} . The maximum value for each plot is (a) 4.37; (b) 2.67; (c) 1.35×10^{-2} ; (d) 6.91; (e) 4.62×10^{-5} ; (f) 64.2; (g) 4.30; (h) 52.3.

contour plot for the summation of all components, R (figure 15g,h) with figure 13 illustrates that the most energetic portion of the separated shear layer contributes more significantly to sound production in the forward step case than in the backward step case (note that the maximum turbulent kinetic energy for the forward step occurs at $x/h = 0.2$, figure 4b, while that for the backward step occurs at $x/h = 4.0$, figure 3b). For both steps, the reattachment regions are relatively unimportant for sound generation because they are located far away from the step corner.

Jacob *et al.* (2001) found, using a source localization technique based on monopoles, that the maximum source region for their backward step coincided with the location of maximum turbulent kinetic energy in the separated shear layer. This is consistent with the raw source distributions shown in figures 13 and 14, but is not representative of the truly important sources in this flow. The results in figure 15 demonstrate the importance of source identification with the appropriate Green's function, which takes into account the diffraction effect of solid boundaries and the increased radiation efficiency.

5. Effect of step height on sound generation

The step height considered so far is a significant portion (53 %) of the boundary layer thickness. Surface discontinuities of much smaller sizes are often found in practical applications, and it is of interest to investigate their effects on sound generation. Six additional simulations consisting of backward and forward steps of

Case	h/δ	h^+	Re_h
1	0.53	786	21 000
2	0.13	197	5250
3	0.033	49	1313
4	0.0083	12	328

TABLE 1. Different step heights and relevant flow parameters. Step heights are successively reduced to 1/4 of the previous one, while the upstream boundary layer is identical. The boundary-layer properties (δ and u_τ) are based on an unperturbed turbulent boundary layer at the step location. For each step height, both backward and forward steps are considered.

three smaller heights were carried out. Table 1 summarizes the parameters for all simulations including the baseline simulations. The additional step heights are 13 %, 3.3 % and 0.83 % of the boundary layer thickness, which remains the same for all cases. In terms of the boundary layer inner scaling, these step heights correspond to 197, 49 and 12 wall units. The first two steps are located in the logarithmic region and the smallest one is in the buffer region of turbulent boundary layer. Computational methods for flow and acoustics are identical to those for the baseline simulations and the same grid resolution is maintained for all cases. The computational domain size for these simulations is the same as in the baseline case in the spanwise direction but is reduced in the streamwise and wall-normal directions because of smaller step heights. In terms of boundary layer thickness, the domain size is $L_x = 10.6\delta$, $L_y = 6.4\delta$ and $L_z = 2.1\delta$. For ease of reference in the rest of the paper, the simulations are labelled as follows: B01, B04, B16, B64, F01, F04, F16, F64, where ‘B’ and ‘F’ stand for backward and forward steps, respectively, and the largest step corresponds to ‘01’ and the smallest to ‘64’ (1/64 of the largest step).

Figure 16 shows the instantaneous streamwise velocity field near the step for all steps. The coordinates are normalized by the step height h , so that as h decreases the plots capture a smaller fraction of the boundary layer and the flow structures appear larger. As the step size decreases from 53 % to 0.83 % of the boundary layer thickness, the flow is less perturbed by the step, and there are fewer flow structures generated by the step. For the largest step height (figure 16a,b), backward and forward facing steps have very different flows near the step as evidenced by the location and extent of separated shear layer and recirculation bubble. In contrast, flows around the smallest steps (figure 16g,h) look similar, implying the incoming flow is very little altered by the steps. The extent of flow structures generated by the steps is further illustrated in figure 17, which depicts the mean streamlines. As the backward step height is reduced, the primary separation bubble becomes more elongated in the streamwise direction relative to the step height, and the secondary recirculation region at the lower step corner disappears. For the forward steps, decreases in the step size lead to disappearance of the recirculation bubble above the step upper surface and much weakened separated shear layer (figure 17f,h). The recirculation zone at the lower step corner increases in size relative to the step height.

Dimensionless frequency spectra of the sound pressure produced by steps of 4 different heights are shown in figure 18 for backward and forward steps. Unlike those in figure 11, the boundary layer thickness δ , instead of h , is used as a length scale for non-dimensionalization. It is common to all steps, and therefore relative sound levels between different steps will remain the same when converted to dimensional quantities. Figure 18 shows that, for a given step height, forward step is louder than

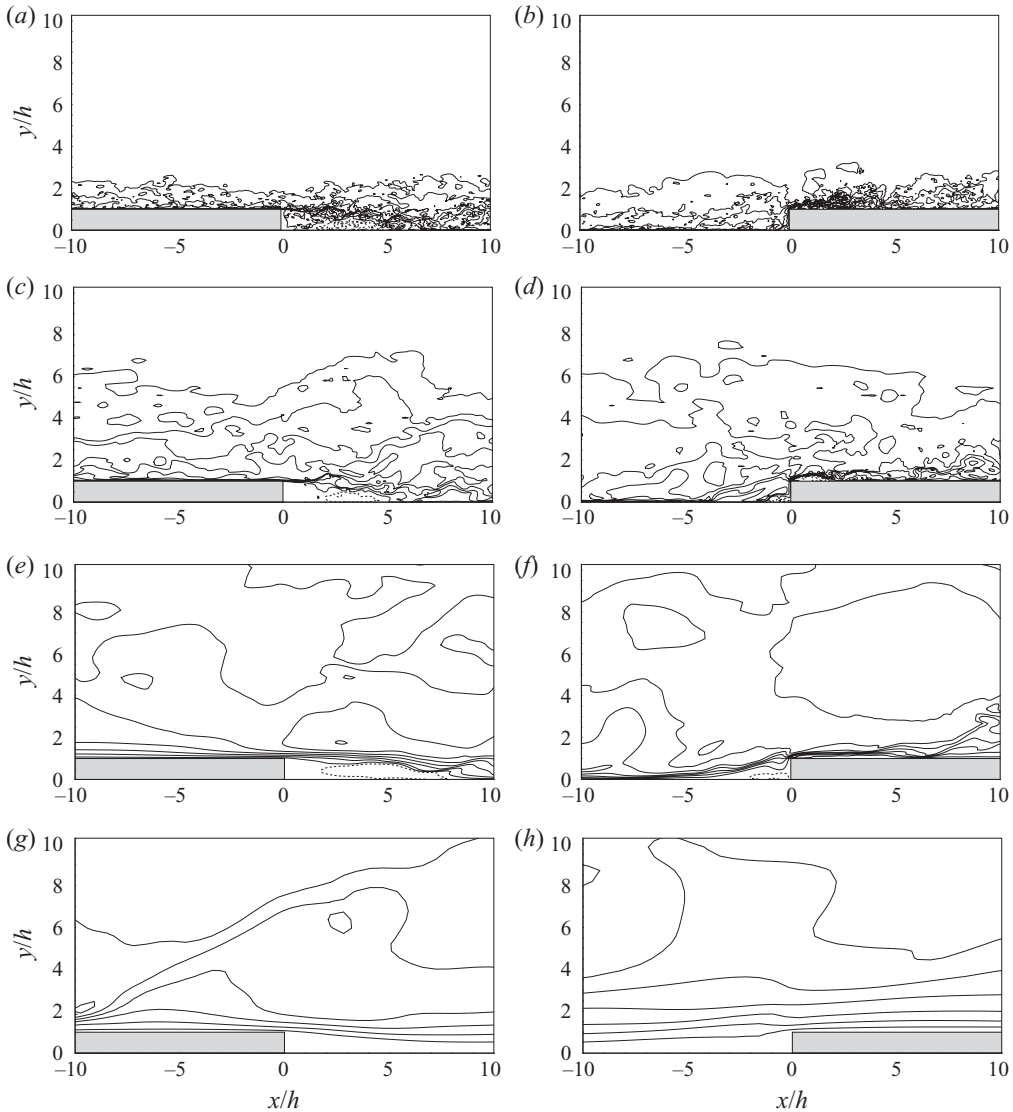


FIGURE 16. Instantaneous streamwise velocity u/U_0 . Ten contour levels are plotted for (a) B01 from -0.224 to 0.930 ; (b) F01 from -0.503 to 1.150 ; (c) B04 from -0.0688 to 0.935 ; (d) F04 from -0.237 to 0.944 ; (e) B16 from -0.0407 to 0.941 ; (f) F16 from -0.0358 to 0.949 ; (g) B64 from 0.0615 to 0.940 ; (h) F64 from 0.0963 to 0.972 . Dotted lines denote negative values.

backward step, but the difference is significantly reduced as the step height decreases. The peak value for the smallest forward step (F64) is only 1.5 dB larger than that for the smallest backward step (B64), compared to a difference of 19 dB between the largest forward and backward steps. For both backward and forward steps, the frequency corresponding to the spectral peak shifts to lower values as the step height increases.

To explain the above observations of sound pressure spectra for backward and forward steps of different sizes, the acoustic source terms are examined in conjunction with the Green's functions for the steps. Figure 19 shows the spatial variation of the

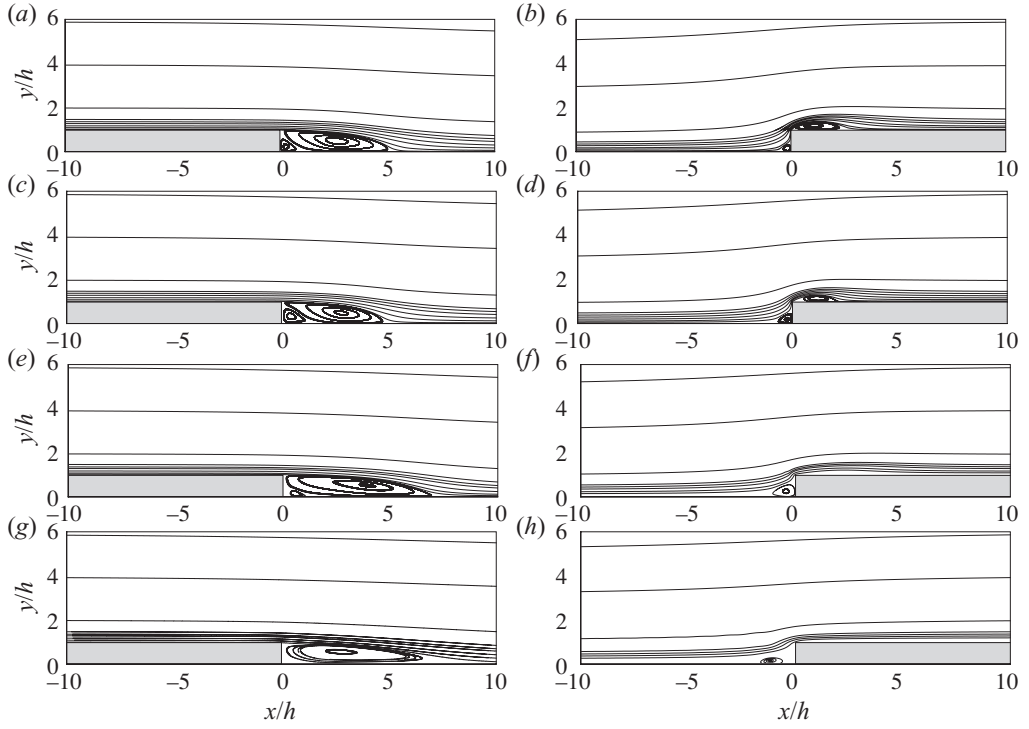


FIGURE 17. Mean streamlines for (a) B01; (b) F01; (c) B04; (d) F04; (e) B16; (f) F16; (g) B64; (h) F64.

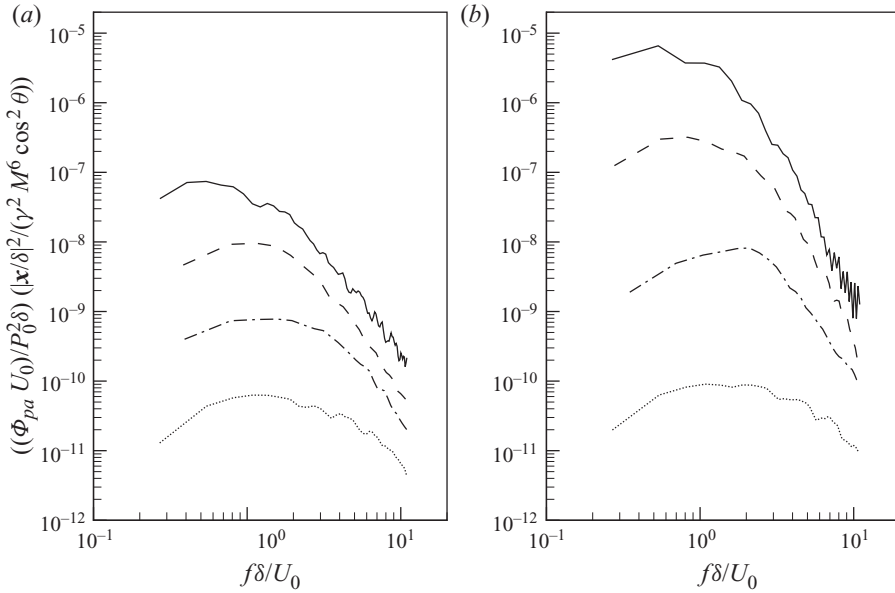


FIGURE 18. Dimensionless sound pressure spectra for four different step heights: (a) backward facing step; (b) forward facing step. —, B(F)01; ----, B(F)04; - · - ·, B(F)16; ·····, B(F)64.

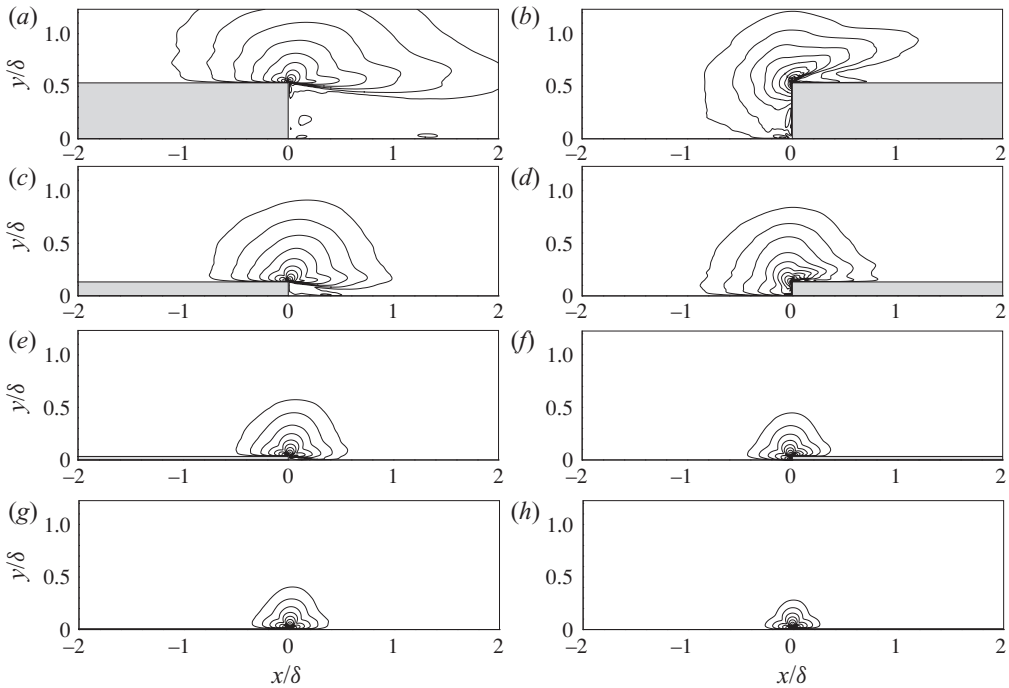


FIGURE 19. Spatial variation of the mean square of Green's function weighted Lighthill stress $\overline{R^2}/(\rho_0 U_0^2)^2$ in (4.12). Thirteen contour levels are plotted in logarithmic scale between maximum and maximum $\times 10^{-6}$, where the maximum values are (a) B01, 9.68; (b) F01, 77.7; (c) B04, 4.16; (d) F04, 6.04; (e) B16, 1.62; (f) F16, 5.48; (g) B64, 0.445; (h) F64, 1.66.

mean square of the Green's function weighted source $R = R_{11} + R_{12} + R_{22}$ in (4.12) for all steps. The contour levels are displayed in logarithmic scale from each step's respective maximum for a six-decade drop in magnitude. The contour shape for the largest steps (figure 19a,b) is similar to that shown earlier for a single frequency (figure 15g,h). As the step size decreases, the weighted source distribution becomes more symmetric about the step vertical face and looks more similar between backward and forward steps. This is because smaller steps cause less distortions to the near-wall flow and the flow field is closer to that of an equilibrium turbulent boundary layer (figure 16). Figure 19 also illustrates that the source regions become more compact as the step size is reduced. This is due to the Green's function, which is more compact for smaller steps when normalized on a common length scale such as δ .

The preceding source analysis based on the frequency spectra and mean square of $R_{ij}(y_1, y_2, t)$ reveals the spatial distribution of Green's function weighted acoustic source magnitude, but provides no information about cancellations that may occur among different source regions. To gain more insight into source processes including potential spatial cancellations, we note that, from (4.7),

$$\begin{aligned} \overline{D^2(t)} &= \iint \overline{D(t) \frac{\partial^2 Y_1}{\partial y_i \partial y_j} Q_{ij}(y_1, y_2, t)} dy_2 dy_1 \\ &= \iiint \iint \frac{\partial^2 Y_1}{\partial y_i \partial y_j} \frac{\partial^2 Y_1}{\partial y'_i \partial y'_j} \overline{Q_{ij}(y_1, y_2, t) Q_{ij}(y'_1, y'_2, t)} dy'_2 dy'_1 dy_2 dy_1, \end{aligned}$$

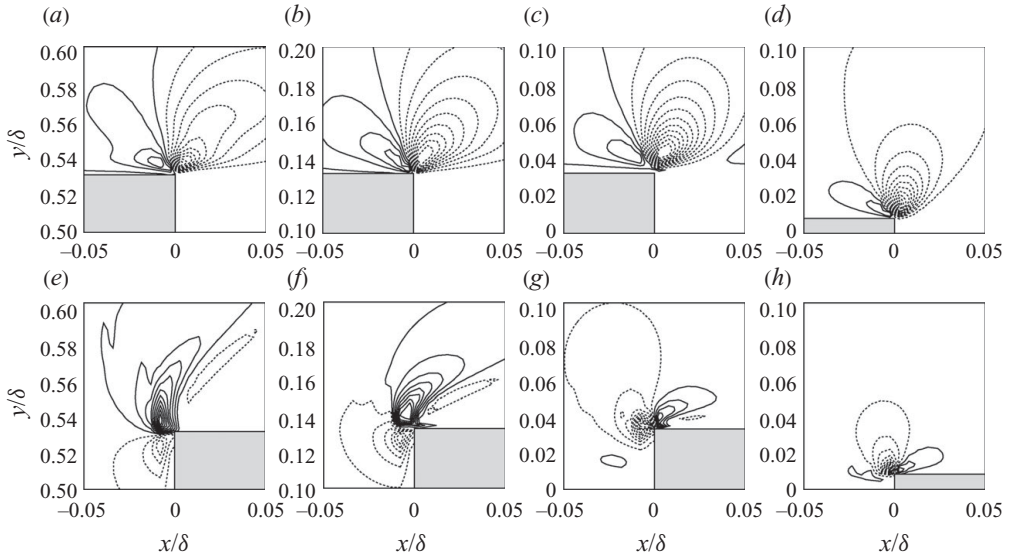


FIGURE 20. Spatial variation of $S(y_1, y_2)/(\rho_0 U_0^2 \delta)^2$ defined in (5.1). Sixteen contour levels are plotted between: (a) B01, -2.16×10^{-4} and 8.10×10^{-5} ; (b) B04, -4.69×10^{-5} and 1.74×10^{-5} ; (c) B16, -5.53×10^{-6} and 1.43×10^{-6} ; (d) B64, -2.25×10^{-6} and 5.19×10^{-7} ; (e) F01, -2.64×10^{-2} and 5.92×10^{-2} ; (f) F04, -2.31×10^{-3} and 2.90×10^{-3} ; (g) F16, -2.06×10^{-4} and 9.58×10^{-5} ; (h) F64, -1.26×10^{-5} and 3.79×10^{-6} . Dotted lines denote negative values.

where the overbar denotes time average. By letting

$$S(y_1, y_2) = \overline{D(t) \frac{\partial^2 Y_1}{\partial y_i \partial y_j} Q_{ij}(y_1, y_2, t)}, \quad (5.1)$$

we obtain

$$\overline{D^2(t)} = \int \int S(y_1, y_2) dy_2 dy_1 = \int \Phi_D(\omega) d\omega,$$

and $\overline{D^2(t)}$ is directly related to the sound power via (4.9). Therefore, $S(y_1, y_2)$ can be used to identify important regions that contribute to the radiated sound power, with account for spatial cancellations.

Figure 20 shows the spatial variation of $S(y_1, y_2)$ in the close vicinity of the step upper corner. Coordinates are scaled by a common length scale δ , and hence, step heights differ as indicated by the ordinate values. Note that the sign of S varies throughout the domain, which leads to considerable cancellations of contributions from different regions to the acoustic source power $\overline{D^2(t)}$. The cancellations near the step tip, where the Green's function weighted sources are strongest, make weaker source regions further away from the tip rise in importance, although the overall effective source region is still quite small due to rapid decay of the Green's function. Relative magnitudes of the maximum contour levels are consistent with the sound pressure spectra shown in figure 18; they are larger for forward steps and for larger step heights. All backward steps and the smallest forward step (F64) display similar contour shapes, implying that their dominant source processes are of similar nature. Furthermore, the contour lines for backward steps are seen above the step upper surface, where the flow is almost identical for all backward steps (i.e. prior to or

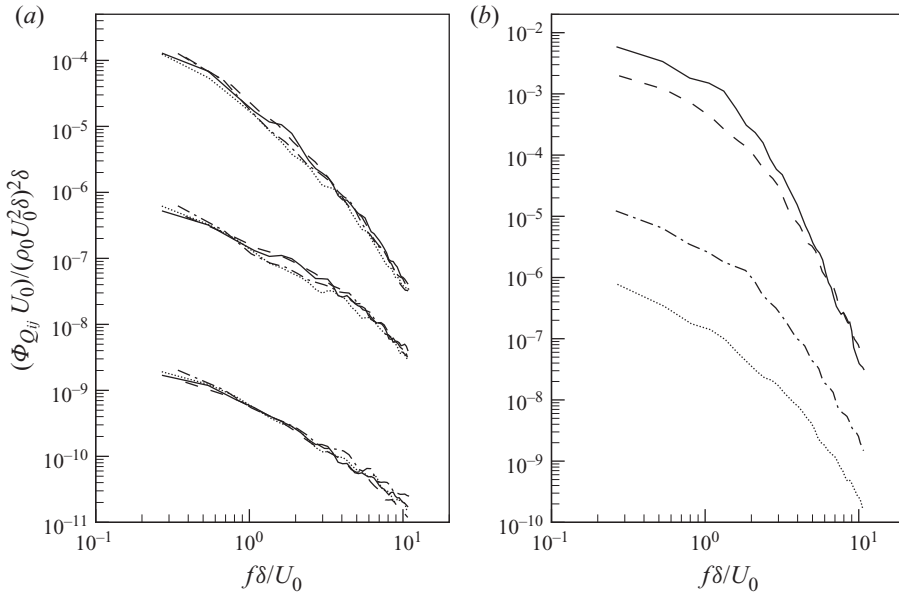


FIGURE 21. Dimensionless frequency spectra of Lighthill stresses at the location of maximum Green's function weighted source strength. (a) Backward facing step: top curves, Q_{11} ; middle curves, $Q_{12} + Q_{21} = 2Q_{12}$; bottom curves, Q_{22} . (b) Forward facing step: Q_{22} only. —, B(F)01; ----, B(F)04; — · —, B(F)16; ·····, B(F)64.

just after separation). The structures arising from flow separation (shear layer and separation bubble) play a lesser role in producing sound as discussed previously. In contrast, the contour shapes for forward steps are more dependent on the step height. For the two largest forward steps (F01 and F04), the important source regions are oriented in the vertical direction (i.e. along the step vertical face), suggesting a strong contribution of the vertical flow in front of the step.

Figure 21 shows the frequency spectra of spanwise integrated Lighthill stresses Q_{ij} at locations that correspond to the maximum contour levels in figure 19. All components of Lighthill stresses are shown for backward steps, while only the Q_{22} component is shown for forward steps for clarity. Q_{22} varies the most among forward steps of different sizes, followed by Q_{12} and Q_{11} . Each component of Lighthill stresses is very similar for all backward facing steps (figure 21a). This is expected, as the spatial location is very near the step upper corner. For the forward steps (figure 21b), the flow condition near the step upper corner is strongly dependent on the height because different step heights correspond to different regions inside the incoming boundary layer, and more importantly because there is a large vertical velocity component induced by the step which becomes stronger with an increasing step height.

Based on the above analyses of acoustic source mechanisms, the sound pressure spectra in figure 18 can be explained as follows. For the backward facing step, the difference in sound pressure level among steps of varying sizes is mainly caused by the Green's function. Important source regions are near the step upper corner, and the flow in this area is similar regardless of the step height. On the other hand, the Green's function is more compact for smaller steps and decays faster away from the step, causing the effective source region to be smaller for the similar sources. For the forward facing step, the disparity in sound level between steps of different heights is caused by not only the Green's function but also the acoustic source, which is

heavily modified by the step. The Lighthill stress component associated with vertical velocity increases significantly as the step height is increased. For the same step height (say, B01 and F01), acoustic source strength is responsible for different sound levels between backward and forward steps.

6. Role of diffraction

Similarities of the flow near the step upper corner among all backward steps (figure 20*a–d*, and figure 21*a*) suggest that important source terms are relatively insensitive to the step height, and that the sound generation is dominated by the Green's function effect, or acoustic diffraction. As mentioned previously, acoustic source mechanisms for flow over surface irregularities can be classified into two broad categories: diffraction and turbulence modification (see e.g. Howe 1989; Yang & Wang 2009). The former is caused by the diffraction of the unsteady hydrodynamic pressure by surface inhomogeneity through the Green's function, and is present even if the flow is not affected by the surface inhomogeneity. To check if the backward step is diffraction-dominated, a numerical experiment is carried out in which the step flow is replaced by an equilibrium turbulent boundary layer over the backward step in the sound calculation. In this hypothetical flow, the turbulent boundary layer continues downstream of the backward step at the same height as the step as though the step did not exist. This is reasonable because, as seen in figure 17, the mean streamlines shortly after separation (in the important source region) are nearly parallel continuations of those in the boundary layer. Lighthill stresses obtained from LES of the flat-plate boundary layer are used together with the Green's function for the backward step to compute the sound source via (4.7). The sound calculated in this manner removes the effect of source field modification (turbulence distortion and generation) by the step and is therefore representative of diffraction sound. The approach described above is analogous to the analytical approach taken by Howe (1989, 1998), who calculated the sound produced via diffraction of frozen boundary-layer pressure field over steps.

Figure 22 compares the frequency spectra of the sound produced by the real and hypothetical flows over backward facing steps of different heights. The differences between the real and hypothetical flows are relatively small (no more than 2.5 dB), and suggest that the sound produced by the backward facing steps may be crudely approximated using source terms from an equilibrium boundary layer in the frequency range considered. In other words, the backward step sound is indeed dominated by diffraction for all step sizes, and the turbulence modification by the step is small. As can be observed in figure 16, the flow structures immediately downstream of the backward steps are not much different from those in the upstream boundary layer. Morris & Foss (2003) observe experimentally that outside a 'subshear layer', which is thin near the step, the turbulence statistics following a backward step represent a continuation of the upstream boundary layer. Furthermore, note that in figure 22 the diffraction-based calculation captures the basic trend in the shift of peak frequency, which becomes lower as the step height increases. This is entirely due to the Green's function; it decays slower for a larger step height, and more eddies of larger size (lower frequency) present in the upper part of the boundary layer participate in sound production.

The same diffraction analysis is not performed for forward facing steps because it is difficult to define a hypothetical 'frozen' source field. The streamlines in figure 17 are severely bent near the forward steps, making passive convection less realistic. Nonetheless, some inferences about the relative importance of diffraction and source

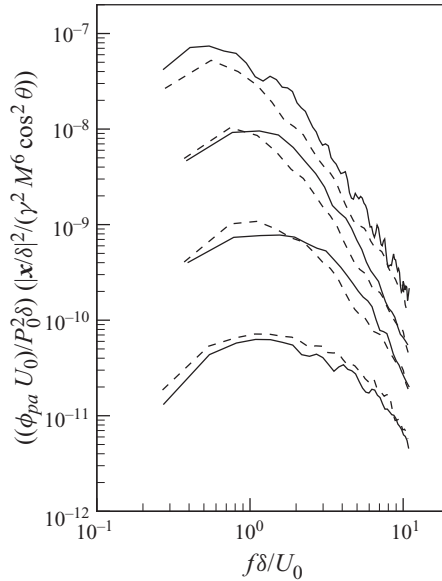


FIGURE 22. Comparison between sound spectra produced by realistic backward facing step flows and by hypothetical backward facing step flows with source terms from an equilibrium turbulent boundary layer. From top to bottom in pairs: B01, B04, B16 and B64. —, source from backward facing step flows; ----, source from equilibrium boundary-layer flows.

modification can be drawn by a comparison with the backward step cases. For the smallest step ($h^+ = 12$), which is located in the buffer region of the boundary layer, the sound spectrum is only slightly higher than the backward-step spectrum, and the flow field is not much perturbed by the step (cf. figure 16*h*). Hence, diffraction is the major mechanism for sound production. As the step height increases, the increase in sound spectral level far exceeds the corresponding increase for backward steps, which is representative of diffraction effects. Thus, turbulence generation and modification by the steps play a major role for the three larger forward facing steps. They produce strong source fields near the steps, which lead to strong sound radiation through diffraction. This conclusion is also supported by the behaviour of source distributions shown in figure 20.

7. Conclusion

LESs of turbulent boundary-layer flow over forward and backward facing steps have been carried out to study sound generation. The Reynolds number based on the step height varies from 21 000 to 328 as the step height changes from 53 % to 0.83 % of the boundary layer thickness. The predicted wall pressure fluctuations from the largest step simulations agree well with the experimental measurements of Farabee & Casarella (1984, 1986) in terms of the r.m.s. values and frequency spectra.

Sound generated by the steps was computed using Lighthill's theory with an approximate Green's function for an acoustically compact step height (Howe 2003), which is valid for low-Mach-number flows over a wide range of frequencies. The use of analytical Green's function allowed the acoustically important source regions to be readily identified and analysed. The steps act primarily as a dipole source aligned in the streamwise direction as indicated by Howe (1989). In agreement with experimental

findings of Farabee & Zoccola (1998), the flow over a forward step emits sound that is significantly stronger than that from a backward step for step heights exceeding the buffer layer. This is because the acoustic source terms are larger in magnitude and located closer to the upper corner of the step where they are weighted heavily by the Green's function.

The effect of step height on radiated sound pressure was studied with four different step heights. Detailed analyses of flow field and Green's function weighted acoustic sources reveal different source mechanisms for the backward and forward steps, which explain the different step height dependence of sound pressure levels. The sound generation by the backward step is dominated by diffraction of the boundary layer source field which is not much affected by the step in the acoustically important region. The Green's function is the main cause for differing sound levels among backward steps of different sizes. For forward steps, different sound levels from varying step heights are attributed to not only diffraction (the Green's function) but also, more importantly, the acoustic source modification by the step, most notably associated with the strong vertical velocity in front of the step. As the step height decreases, source modification becomes less significant, and sound spectrum approaches that of the backward step in the diffraction limit.

This work was supported by the Office of Naval Research under Grants N00014-06-1-0640 (program officer: Dr Ki-Han Kim) and N00014-09-1-0602 (program officer: Dr Ronald Joslin). Computer time was provided by the US Department of Defense High Performance Computing Modernization Program (HPCMP) through the Naval Research Laboratory Affiliated Resource Center. We gratefully acknowledge Dr William K. Blake and Dr Donghyun You for valuable discussions. Portions of this work were presented as AIAA-2008-3052 at the Fourteenth AIAA/CEAS Aeroacoustics Conference, Vancouver, British Columbia, 5-7 May, 2008, and as AIAA-2010-0006 at the Forty-eighth AIAA Aerospace Sciences Meeting, Orlando, Florida, 4-7 January, 2010.

Appendix. Evaluation of the Lighthill integral in §4.1

When $G(\mathbf{x}, \omega; \mathbf{y})$ in (4.4) is differentiated twice with respect to \mathbf{y} , we obtain

$$\left. \begin{aligned} \frac{\partial^2 G}{\partial y_i \partial y_j} &= \frac{1}{4\pi} \frac{\partial^2}{\partial y_i \partial y_j} \left(\frac{e^{ikr}}{r} + \frac{e^{ikr'}}{r'} \right) \\ &= \frac{e^{ikr}}{4\pi r^2} \left\{ -ikr_m \frac{\partial^2 Y_m}{\partial y_i \partial y_j} - k^2 \frac{r_l r_m}{r} \frac{\partial Y_l}{\partial y_j} \frac{\partial Y_m}{\partial y_i} + \frac{r_m}{r} \frac{\partial^2 Y_m}{\partial y_i \partial y_j} - ik \frac{3r_l r_m}{r^2} \frac{\partial Y_l}{\partial y_j} \frac{\partial Y_m}{\partial y_i} \right. \\ &\quad \left. + ik \frac{\partial Y_l}{\partial y_i} \frac{\partial Y_l}{\partial y_j} + \frac{3r_l r_m}{r^3} \frac{\partial Y_l}{\partial y_j} \frac{\partial Y_m}{\partial y_i} - \frac{1}{r} \frac{\partial Y_l}{\partial y_i} \frac{\partial Y_l}{\partial y_j} \right\} \\ &\quad + \frac{e^{ikr'}}{4\pi r'^2} \left\{ -ikr'_m \frac{\partial^2 Y'_m}{\partial y_i \partial y_j} - k^2 \frac{r'_l r'_m}{r'} \frac{\partial Y'_l}{\partial y_j} \frac{\partial Y'_m}{\partial y_i} + \frac{r'_m}{r'} \frac{\partial^2 Y'_m}{\partial y_i \partial y_j} - ik \frac{3r'_l r'_m}{r'^2} \frac{\partial Y'_l}{\partial y_j} \frac{\partial Y'_m}{\partial y_i} \right. \\ &\quad \left. + ik \frac{\partial Y'_l}{\partial y_i} \frac{\partial Y'_l}{\partial y_j} + \frac{3r'_l r'_m}{r'^3} \frac{\partial Y'_l}{\partial y_j} \frac{\partial Y'_m}{\partial y_i} - \frac{1}{r'} \frac{\partial Y'_l}{\partial y_i} \frac{\partial Y'_l}{\partial y_j} \right\}. \end{aligned} \right\} \quad (\text{A } 1)$$

The quadrupole terms can be neglected based on the compact step height approximation: $kh \ll 1$. Furthermore, for an observer located in the acoustic and hydrodynamic far field ($kr \gg 1$ and $r \gg h$), we retain only the leading-order terms in

1/r,

$$\frac{1}{4\pi} \frac{\partial^2}{\partial y_i \partial y_j} \left(\frac{e^{ikr}}{r} + \frac{e^{ikr'}}{r'} \right) \approx \frac{e^{ikr}}{4\pi r^2} \left(-ikr_m \frac{\partial^2 Y_m}{\partial y_i \partial y_j} \right) + \frac{e^{ikr'}}{4\pi r'^2} \left(-ikr'_m \frac{\partial^2 Y'_m}{\partial y_i \partial y_j} \right). \quad (\text{A } 2)$$

From (4.4), the only non-zero terms of $\partial^2 Y_m / \partial y_i \partial y_j$ and $\partial^2 Y'_m / \partial y_i \partial y_j$ are those with $m = 1$ and $i, j = 1$ and 2 . Recognizing that $r_1 = r'_1$ and $Y_1 = Y'_1$, we arrive at (4.5),

$$\frac{\partial^2 G}{\partial y_i \partial y_j} = -\frac{ikr_1}{4\pi} \left(\frac{e^{ikr}}{r^2} + \frac{e^{ikr'}}{r'^2} \right) \frac{\partial^2 Y_1}{\partial y_i \partial y_j}. \quad (\text{A } 3)$$

Substituting (A 3) into the volume integral in (4.2) and noting that $r_1 = r \cos \theta$ (θ is the angle between \mathbf{r} and positive x -axis) and $r \approx |\mathbf{x}| \approx r'$ for a compact source lead to

$$\hat{p}(\mathbf{x}, \omega) = \int_V \hat{T}_{ij}(\mathbf{y}, \omega) \frac{\partial^2 G}{\partial y_i \partial y_j}(\mathbf{x}, \omega; \mathbf{y}) \, d^3 \mathbf{y} \approx -\frac{ik}{2\pi} \frac{e^{ik|\mathbf{x}|} \cos \theta}{|\mathbf{x}|} \int_V \hat{T}_{ij}(\mathbf{y}, \omega) \frac{\partial^2 Y_1}{\partial y_i \partial y_j} \, d^3 \mathbf{y}.$$

Further, noting that $\partial^2 Y_1 / \partial y_i \partial y_j$ is a function of y_1 and y_2 only, we obtain (4.6),

$$\begin{aligned} \hat{p}(\mathbf{x}, \omega) &\approx -\frac{ik}{2\pi} \frac{e^{ik|\mathbf{x}|} \cos \theta}{|\mathbf{x}|} \frac{1}{2\pi} \int \int \int \frac{\partial^2 Y_1}{\partial y_i \partial y_j} \int T_{ij}(\mathbf{y}, t) \, dy_3 dy_2 dy_1 e^{i\omega t} \, dt \\ &= -\frac{ik}{2\pi} \frac{e^{ik|\mathbf{x}|} \cos \theta}{|\mathbf{x}|} \hat{D}(\omega), \end{aligned} \quad (\text{A } 4)$$

where

$$D(t) = \int \int \frac{\partial^2 Y_1}{\partial y_i \partial y_j} Q_{ij}(y_1, y_2, t) \, dy_2 \, dy_1$$

and

$$Q_{ij}(y_1, y_2, t) = \int T_{ij}(\mathbf{y}, t) \, dy_3.$$

The function $Y_1(y_1, y_2)$ is obtained by solving an equivalent potential flow problem with Schwartz–Christoffel transformation. The transformation from the physical Z -plane ($Z = y_1 + iy_2$) to the transformed ζ -plane ($\zeta = \xi + i\eta$), which maps the points $Z = 0$ and $Z = ih$ into $\zeta = -1$ and $\zeta = 1$, respectively, is given by

$$Z = \frac{h}{\pi} \left\{ \pm \ln(i\zeta + \sqrt{1 - \zeta^2}) + i\sqrt{1 - \zeta^2} \right\} + i\frac{h}{2}, \quad (\text{A } 5)$$

where h is the step height. The negative sign in front of the natural logarithm is for the transformation for the backward step, which maps $Z = ih$ and $Z = 0$ into $\zeta = -1$ and $\zeta = 1$, respectively. The complex potential W in the ζ -plane with free-stream velocity U_0 is

$$W(\zeta) = Y_1 + i\Psi = \frac{U_0 h}{\pi} \zeta, \quad (\text{A } 6)$$

where Y_1 and Ψ are analogous to the velocity potential and stream function, respectively, in a potential flow.

REFERENCES

ADDAD, Y., LAURENCE, D., TALOTTE, C. & JACOB, M. C. 2003 Large eddy simulation of a forward-backward facing step for acoustic source identification. *Intl J. Heat Fluid Flow* **24**, 562–571.

- AKSELVOLL, K. & MOIN, P. 1995 Large eddy simulation of turbulent confined coannular jets and turbulent flow over a backward facing step. *Tech. Rep.* TF-63. Department of Mechanical Engineering, Stanford University, Stanford, CA.
- ALI, I., KREY, F., BECKER, S., MUNZ, C.-D. & UTMANN, J. 2007 Coupling of LES with LEE for forward facing step noise prediction. *Paper* 2007-3507. AIAA.
- BADRI NARAYANAN, M. A., KHADGI, Y. N. & VISWANATH, P. R. 1974 Similarities in pressure distribution in separated flow behind backward-facing steps. *Aeronaut. Q.* **25**, 305-312.
- BECKER, S., ESCOBAR, M., HAHN, C., ALI, I., KALTENBACHER, M., BASEL, B. & GRÜNEWALD, M. 2005 Experimental and numerical investigation of the flow induced noise from a forward facing step. *Paper* 2005-3006. AIAA.
- BRADSHAW, P. & WONG, F. Y. F. 1972 The reattachment and relaxation of a turbulent shear layer. *J. Fluid Mech.* **52**, 113-135.
- CAMUSSI, R., GUI, G. & RAGNI, A. 2006 Wall pressure fluctuations induced by turbulent boundary layers over surface discontinuities. *J. Sound Vib.* **294**, 177-204.
- CHANDRSUDA, C. & BRADSHAW, P. 1981 Turbulent structure of a reattaching mixing layer. *J. Fluid Mech.* **110**, 171-179.
- CHERRY, N. J., HILLIER, R. & LATOUR, M. E. M. P. 1984 Unsteady measurements in a separated and reattaching flow. *J. Fluid Mech.* **144**, 13-46.
- CONLISK, A. T. & VELEY, D. 1985 The generation of noise in impinging vortex motion past a step. *Phys. Fluids* **28**, 3004-3012.
- CRIGHTON, D. G. 1975 Basic principles of aerodynamic noise generation. *Prog. Aerosp. Sci.* **16**, 31-96.
- DHANAK, M. R. & GUNDLAPALLI, R. 1992 Flow noise due to interaction between an eddy and a forward facing step. In *International Symposium of Flow Induced Vibration and Noise* (ed. T. M. Farabee & M. P. Paidoussis), Flow-Structure and Flow-Sound Interactions, vol. 3, pp. 11-22. ASME.
- EATON, J. K. & JOHNSTON, J. P. 1981 A review of research on subsonic turbulent flow reattachment. *AIAA J.* **19**, 1093-1100.
- EFIMTSOV, B. M., KOZLOV, N. M., KRAVCHENKO, S. V. & ANDERSSON, A. O. 1999 Wall pressure fluctuation spectra at small forward facing steps. *Paper* 99-1964. AIAA.
- EFIMTSOV, B. M., KOZLOV, N. M., KRAVCHENKO, S. V. & ANDERSSON, A. O. 2000 Wall pressure fluctuation spectra at small backward facing steps. *Paper* 2000-2053. AIAA.
- FADLUN, E. A., VERZICCO, R., ORLANDI, P. & MOHD-YUSOF, J. 2000 Combined immersed-boundary finite-difference methods for three-dimensional complex flow simulations. *J. Comput. Phys.* **161**, 35-60.
- FARABEE, T. M. & CASARELLA, M. J. 1984 Effects of surface irregularity on turbulent boundary layer wall pressure fluctuations. *ASME J. Vib., Acoust., Stress Reliab. Des.* **106**, 343-350.
- FARABEE, T. M. & CASARELLA, M. J. 1986 Measurements of fluctuating wall pressure for separated/reattached boundary layer flows. *ASME J. Vib., Acoust., Stress Reliab. Des.* **108**, 301-307.
- FARABEE, T. M. & ZOCCOLA, P. J. 1998 Experimental evaluation of noise due to flow over surface steps. In *Proceedings of the ASME International Mechanical Engineering Congress Exposition 1998*, vol. 25, pp. 95-102.
- GERMANO, M., PIOMELLI, U., MOIN, P. & CABOT, W. H. 1991 A dynamic subgrid-scale eddy-viscosity model. *Phys. Fluids A* **3**, 1760-1765.
- GOLDSTEIN, M. E. 1976 *Aeroacoustics*, 2nd edn. McGraw-Hill.
- HOWE, M. S. 1989 Sound produced by turbulent boundary layer flow over a finite region of wall roughness, and over a forward facing step. *J. Fluids Struct.* **3**, 83-96.
- HOWE, M. S. 1997 Influence of separation on sound generated by vortex-step interaction. *J. Fluids Struct.* **11**, 857-872.
- HOWE, M. S. 1998 On the contribution from skin steps to boundary-layer generated interior noise. *J. Sound Vib.* **209**, 519-530.
- HOWE, M. S. 2003 *Theory of Vortex Sound*. Cambridge University Press.
- JACOB, M. C., LOUISOT, A., JUVE, D. & GUERRAND, S. 2001 Experimental study of sound generated by backward-facing steps under wall jet. *AIAA J.* **39**, 1254-1260.

- KARGUS, W. A., IV & LAUCHLE, G. C. 1997 Flow-induced sound from turbulent boundary layer separation over a rearward facing step. *Tech. Rep.* Report TR 97-007. Applied Research Laboratory. Penn State University.
- KIM, J. & SUNG, H. J. 2006 Wall pressure fluctuations and flow-induced noise in a turbulent boundary layer over a bump. *J. Fluid Mech.* **558**, 79–102.
- KIYA, M. & SASAKI, K. 1983 Structure of a turbulent separation bubble. *J. Fluid Mech.* **137**, 83–113.
- LARGEAU, J. F. & MORINIERE, V. 2007 Wall pressure fluctuations and topology in separated flows over a forward-facing step. *Exp. Fluids* **42**, 21–40.
- LAUCHLE, G. C. & KARGUS, W. A., IV 2000 Scaling of turbulent wall pressure fluctuations downstream of a rearward facing step. *J. Acoust. Soc. Am.* **107**, L1–L6.
- LE, H., MOIN, P. & KIM, J. 1997 Direct numerical simulation of turbulent flow over a backward-facing step. *J. Fluid Mech.* **330**, 349–374.
- LECLERCQ, D. J. J., JACOB, M. C., LOUISOT, A. & TALOTTE, C. 2001 Forward-backward facing step pair: aerodynamic flow, wall pressure and acoustic characterization. *Paper* 2001–2249. AIAA.
- LEE, I. & SUNG, H. J. 2001 Characteristics of wall pressure fluctuations in separated and reattaching flows over a backward-facing step. Part I. Time-mean statistics and cross-spectral analyses. *Exp. Fluids* **30**, 262–272.
- LIGHTHILL, M. J. 1952 On sound generated aerodynamically. Part I. General theory. *Proc. R. Soc. Lond. Ser. A* **211**, 564–587.
- LILLY, D. K. 1992 A proposed modification of the Germano subgrid-scale closure model. *Phys. Fluids A* **4**, 633–635.
- LUND, T. S., WU, X. & SQUIRES, K. D. 1998 Generation of turbulent inflow data for spatially-developing boundary layer simulations. *J. Comput. Phys.* **140**, 233–258.
- MOHSEN, A. M. 1968 Experimental investigation of the wall pressure fluctuations in subsonic separated flows. *Tech. Rep.* No. D6-17094. Boeing Company Report.
- MORRIS, S. C. & FOSS, J. F. 2003 Turbulent boundary layer to single-stream shear layer: the transition region. *J. Fluid Mech.* **494**, 187–221.
- MOSS, W. D. & BAKER, S. 1980 Re-circulating flows associated with two-dimensional steps. *Aeronaut. Q.* **151–172**.
- NA, Y. & MOIN, P. 1998 The structure of wall-pressure fluctuations in turbulent boundary layers with adverse pressure gradient and separation. *J. Fluid Mech.* **377**, 347–373.
- WANG, M., FREUND, J. B. & LELE, S. K. 2006 Computational prediction of flow-generated sound. *Annu. Rev. Fluid Mech.* **38**, 483–512.
- WANG, M., LELE, S. K. & MOIN, P. 1996 Computation of quadrupole noise using acoustic analogy. *AIAA J.* **34**, 2247–2254.
- WANG, M. & MOIN, P. 2000 Computation of trailing-edge flow and noise using large-eddy simulation. *AIAA J.* **38**, 2201–2209.
- WANG, M., MOREAU, S., IACCARINO, G. & ROGER, M. 2009 LES prediction of wall-pressure fluctuations and noise of a low-speed airfoil. *Intl J. Aeroacoust.* **8**, 177–198.
- YANG, Q. & WANG, M. 2009 Computational study of roughness-induced boundary layer noise. *AIAA J.* **47**, 2417–2429.
- YOU, D., MOIN, P., WANG, M. & MITTAL, R. 2004 Study of tip clearance flow in a turbomachinery cascade using large eddy simulation. *Tech. Rep.* TF-86. Department of Mechanical Engineering, Stanford University, Stanford, CA.
- YOU, D., WANG, M., MOIN, P. & MITTAL, R. 2007 Large-eddy simulation analysis of mechanisms for viscous losses in a turbomachinery tip-clearance flow. *J. Fluid Mech.* **586**, 177–204.